Efficient shape sensing of plate structures using the inverse Finite Element Method aided by strain pre-extrapolation

Original
Efficient shape sensing of plate structures using the inverse Finite Element Method aided by strain pre-extrapolation / Roy, R., Tessler, A., Surace, C., Gherlone, M.. - In: THIN-WALLED STRUCTURES. - ISSN 0263-8231. - ELETTRONICO. - 180:(2022), p. 109798. [10.1016/j.tws.2022.109798]

Publisher:
Elsevier

Published
DOI:10.1016/j.tws.2022.109798

Efficient Shape Sensing of Plate Structures using the inverse Finite Element Method aided by Strain Pre-extrapolation

Rinto Roy [a,*], Alexander Tessler [b], Cecilia Surace [c], and Marco Gherlone [a]

[a] Politecnico di Torino, Department of Mechanical and Aerospace Engineering, Corso Duca degli Abruzzi 24, 10129 Torino, Italy; rinto.roy@polito.it; marco.gherlone@polito.it

[b] Structural Mechanics and Concepts Branch, NASA Langley Research Center, Mail Stop 190, Hampton, VA 23681-2199, USA; alexander.tessler-1@nasa.gov

[c] Politecnico di Torino, Department of Structural, Geotechnical and Building Engineering, Corso Duca degli Abruzzi 24, 10129 Torino, Italy; cecilia.surace@polito.it

Abstract:

The inverse problem of reconstructing structural deformations based on measured strain data, known as shape sensing, is addressed in this numerical study for a cantilevered plate undergoing complex bending and twisting deformations. The inverse Finite Element Method (iFEM) is the main computational tool used for solving the inverse problem, and the Smoothing Element Analysis (SEA) is used as a pre-processing step seeding additional strain data into a high-fidelity iFEM discretization. This novel SEA-iFEM approach demonstrates that even with a small number of strain sensors and a judicial choice of strain-sensor layouts, accurate shape-sensing reconstructions for plate structures can be obtained.

Keywords: Shape Sensing, Plate Structures, Structural Health Monitoring, inverse Finite Element Method, Strain Pre-extrapolation, Inverse problem.

---

[*] Corresponding author: rinto.roy@polito.it (Rinto Roy)

1. Introduction

Advanced diagnostic and prognostic capabilities are essential for the health management of various aerospace, civil, and marine structures and systems [1]. The aerospace industry has focused on the Integrated Vehicle Health Management (IVHM) framework to enable the maintenance and performance improvements of future aircraft and spacecraft [2,3]. Advancements in sensor technologies have allowed structures to be instrumented with an increasing number of onboard sensors measuring structural response in real time. Several inverse solution methods have been examined that use measured sensor data to assess the real-time structural response and structural integrity. In particular, for the inverse problem of detection, characterisation, and prognosis of damage using measured sensor data, the solution techniques proposed are mainly based on the use of a system model [4]. In such cases, the inverse problem is formulated by combining the measured sensor data with a physics-based computational model (e.g. FEM model) that simulates structural behaviour [5] and is solved by minimising the difference between measured structural response and model predictions. Multiple optimization-based solution strategies exist, an example being stochastic inference methods that use probabilistic descriptions of the model parameters inferred from the measured sensor data [6]. Such model-based techniques, however, suffer from a key limitation – the computational effort required can increase significantly with the increasing complexity of the monitored structure. Strategies have been proposed to address this issue without comprising prediction accuracy, a popular approach being the use of surrogate models to produce reduced representations of large numerical systems. One interesting application is the use of polynomial chaos expansion for developing stochastic surrogate models for dynamic non-linear structural systems [7]. In contrast to these largely data-driven approaches, physics-based approaches have also been examined. One such approach is an extended Finite Element Method (XFEM) [8] which has been recently used for crack detection in 3D structures [4]. Moreover, to reduce the computational effort, neural networks, trained on measured or numerical data, have also been proposed. For example, an FEM-based Deep Neural Network (DNN) approach was demonstrated to predict the non-linear response of hyper-elastic bodies [9].

In recent years, the topic of shape sensing has emerged as a key technology for the real-time structural displacement, strain, stress, and damage monitoring [10]. Shape sensing is defined as the inverse problem of reconstructing structural displacements from discrete surface-strain measurements. This is true not only for traditional vehicles and structures but also for developing shape morphing structures whose form can be varied based on their function [11]. A prime example is the development of morphing aircraft wings [12,13]. This also represents an area of application for shape sensing to monitor and control the deformed configuration of morphing structures [14,15]. As shape sensing also falls within the general category of inverse problems, it is ill-posed and do not necessarily satisfy the conditions of uniqueness and existence of a solution. Within the realm of shape sensing research, solutions have been approached by way of four main approaches: neural networks, approximation of the displacement field using global or piecewise continuous basis functions, use of finite element methods derived from a least-squares variational principle, and numerical integration of experimental strains, [16].

Bruno et al. [17] proposed a neural-network approach for shape sensing using a limited number of on-board measurements. Displacement reconstruction methods using basis functions have also been developed [18–21]. In particular, approaches that adopt the structural mode shapes and some discrete strain measurements have been proposed [18,20]. Development of finite element-based shape-sensing approaches was pioneered by Tessler and Spangler [22,23]. Ko et al. [24] proposed a shape sensing strategy based on strain integration and demonstrated that both bending and torsional response of beams can be reconstructed using axial surface strain measurements. The capabilities of this theory were demonstrated on prismatic and tapered beams, and on complex wing structures [25]. For a comprehensive review of various shape-sensing approaches the interested reader is referred to [16].

This work focuses on the finite element-based shape-sensing approaches, mainly related to the variational principle of Tessler and Spangler [22,23]. In Ref. [22,23], Mindlin plate kinematic assumptions are used in which in-situ strain measurements are required to match, in a least-square sense, with the corresponding analytic strain fields. Consequently, a number of displacement-based finite elements have been developed to form the building blocks of the inverse Finite Element Method (iFEM). A key computational advantage that sets iFEM apart from the other inverse solution approaches described previously is that no system model is required to arrive at accurate predictions of the structural response. Additionally, because iFEM is formulated on the basis of strain-displacement relations only, it is inherently independent of the material properties and operational conditions of the structure. The original iFEM formulation for plate and shell structures employed a three-node inverse shell element (iMIN3) [26]. This element uses C^0-continuous, anisoparametric interpolations that are adopted from a related direct (forward) finite element formulation [27]. Kefal et al. [28] formulated a four-node quadrilateral inverse shell element with drilling degrees-of-freedom (iQS4), and an eight-node curved inverse shell element (iCS8) [29]. Within the iFEM framework, Gherlone et al. [30] developed a set of inverse beam and frame elements and studied their predictive shape-sensing capabilities on beam and frame structures. Roy et al. [31] introduced an inverse-beam formulation capable of treating relatively complex beam cross-sections in an efficient manner.

Recently, iFEM has been used for shape sensing analyses of a composite stiffened panel [32], a composite wing box [33,34], marine applications (a Panamax container ship [35] and bulk carriers [36]), plate structures [37–39], cylindrical stiffened panels [40], and offshore wind turbines [41]. Miller et al. [42], using experimental measurements, demonstrated the use of iFEM for predicting deformations and internal loads on an aircraft wing test article. Gherlone et al. [16], using a wing-shaped aluminum plate with surface strains measured in a mechanics laboratory, performed iFEM shape-sensing calculations and compared several different shape-sensing approaches. Additional experimental iFEM studies, using a moderately thick wing-shaped sandwich structure, have been performed by Kefal et al. [43]. Oboe et al. [44] studied a stiffened panel instrumented with fiber-optic sensors, and Colombo et al. [45] performed an iFEM analysis on a CFRP reinforced panel subjected to impact damage and a compressive fatigue test.

One important aspect of any predictive shape-sensing technique, including iFEM, is the reliance on a suitable array of discretely located strain measurements, where the number and location of the strain sensors can affect the feasibility and accuracy of the displacement reconstruction. Within iFEM, stable and accurate solutions can be obtained even when some elements lack any measured strain data. This is achieved by specifying very small weighting coefficients associated with the least-square terms where such measured strains are missing.

Various attempts have been made to optimize strain-sensor locations to achieve accurate shape sensing predictions. Kefal et al. [46] investigated the effect of sensor spatial density and alignment for iFEM shape sensing of a wing-shaped thick panel subject to various loading conditions. They concluded that sparse uniaxial strain measurement was sufficient for reconstructing the bending response, whereas triaxial strain measurements were sufficient for the torsional response. Esposito et al. [33] used genetic algorithms to optimize strain sensor locations and directions for minimizing iFEM displacement reconstruction errors of a composite wing box. Similarly, Zhao et al. [47] demonstrated optimal sensor placement on a three-dimensional frame using Particle Swarm Optimization (PSO) and on a wing frame using eigenvalue analysis [48]. Roy et al. [49] investigated the use of simple strain sensor patterns to reconstruct the vibration mode shapes of a rectangular plate. A smart system to determine the optimal on-board strain sensors for SHM of ship structures was proposed by Kefal et al. [50].

Optimization-based strain sensor approaches commonly result in somewhat random and complex arrangements of strain sensors. These arrangements are specific to the structural geometry, loading conditions, and the displacement response patterns. Hence, for a given structure and changing loading conditions, such approaches result in completely different strain sensor patterns, making them difficult to apply in practice. To overcome such difficulties, the present research examines relatively simple and cost-effective strain sensor configurations aimed at providing sufficiently accurate shape-sensing predictions under a wide range of loading conditions, material systems, and structural geometries.

The strain senor patterns of Ref. [49] were introduced as a possible solution to this problem. These patterns resemble the shape of commonly used load-bearing frame structures, and the related iFEM performance was investigated on the reconstruction of the vibrational mode shapes of a cantilevered rectangular plate [49]. They comprise of a combination of sensor paths along the plate boundaries and internal plate diagonals, and the proposed relatively simple arrangements of strain sensors ensures that applying them for practical applications remains feasible. iFEM reconstruction using these patterns produced accurate predictions of plate deformation for both low and high vibrational modes of the plate. As their shape sensing performance has been demonstrated and quantified, these patterns can potentially be adapted for more complex structures to develop built-up sensor networks comprising of one or more of these elementary sensor patterns.

Other strategies to overcome issues related to the limited number of strain sensors are interpolation and smoothing of strain data. Tessler et al. [51] proposed a variational method to recover smoothed stresses from a non-smooth finite element stress field. The procedure, referred to as the Smoothing Element Analysis (SEA), discretizes the structural domain using least-squares finite elements, where within each element the variable to be smoothed (e.g., a component of stress, strain, or any other quantity of interest) is interpolated using piecewise continuous functions. SEA is based on minimising a functional defined as the penalised least-squares error between the continuous and discrete values of the quantity analysed. In the present context, the SEA can be used to generate C^1-continuous strains from a set of discrete experimental strain measurements. This continuous strain distribution can contribute additional strain data for the iFEM analysis. In addition to the three-node triangular smoothing element [52,53], a four-node quadrilateral smoothing element was also developed [54]. Following the original pre-processing strategy proposed by Tessler and Spangler [22,23], Kefal et al. [55] used SEA as a pre-processor of in-situ strain data for application to iFEM. They successfully applied this approach for shape sensing of multi-layered composite and sandwich structures. Roy et al. [39] investigated the problem of crack damage identification in a thin plate using uniaxial strain data, where SEA was used as a pre-processor of the in-situ strain data for iFEM. Oboe et al. [56] compared the performance of SEA to polynomial fitting as a strategy for extrapolating strains for iFEM reconstruction of a composite plate subject to buckling. They reported that to obtain accurate results appropriate selection of correct SEA mesh size and hyperparameters were essential.

In this paper, the approach introduced in Ref. [49] is extended with the main goal of reducing the number of strain sensors even further, without a substantial loss of accuracy. The reduction in the number of strain sensors is aimed at reducing the overall cost of instrumentation, thus making this methodology even more appealing for practical applications. To achieve substantial strain sensor reductions, the in-situ strain data are smoothed using frame-like SEA patterns. These strain sensor patterns are combined with smoothed strain data to produce new 'reduced' patterns with fewer number of strain sensors. Investigating suitable SEA models that generate smoothed strain data and assessing iFEM predictions using the new reduced sensor patterns is the focus of this work. A key advantage of the loosely coupled SEA-iFEM approach is that a relatively small number of sensors may be used without assistance from a system model. In this application, the role of SEA is to pre-process a relatively small set of strain measurements to achieve a much larger set of sufficiently accurate strains to be used by iFEM. Neither technique requires any information regarding the material properties nor the operational conditions of the structure.

The remainder of the paper is organized as follows. In Section 2, the theoretical foundation of iFEM is reviewed in the context of SEA pre-processed strain data. In Section 3, a comprehensive computational study is discussed. The focus problem is that of a cantilevered plate that exhibits complex deformation patterns. The deformation patterns examined are those of high frequency vibration modes. Using reduced strain sensor patterns, and SEA assisted strain data pre-processing, the high-fidelity iFEM models are used for full-field displacement reconstruction analysis. Finally, in Section 4, concluding remarks are summarized.

2. Review of iFEM and SEA

Within the conceptual framework of iFEM, the structure, which is undergoing deformations due to arbitrary loading, is discretized with the so-called *inverse* finite elements. The inverse elements are derived from a weighted least-squares variational principle that was originally introduced for Mindlin plates and shells by Tessler and Spangler [22,23]. The iFEM framework has been shown to be computationally efficient and has the advantage of accommodating arbitrary structural configurations and material systems. It allows for a wide range of discretization strategies related to the distribution of in-situ strain data. For shape-sensing (deformed shape) and strain reconstruction, no loading or material information is required for the analysis. For stress resultant and stress reconstruction, Hooke's constitutive relations must be invoked.

Using the kinematic assumptions of Mindlin theory [57], the displacement vector can be expressed in terms of the in-plane (membrane) displacements $u(\mathbf{x})$ and $v(\mathbf{x})$, the transverse displacement (deflection) $w(\mathbf{x})$, and the bending rotations $\theta_x(\mathbf{x})$ and $\theta_y(\mathbf{x})$ about the positive x and y directions, respectfully, where $\mathbf{x} \equiv (x, y)$ denote the midplane orthogonal reference coordinates. The three Cartesian displacement components are given as

$$u_x = u(\mathbf{x}) + z\,\theta_y(\mathbf{x}), \quad u_y = v(\mathbf{x}) - z\,\theta_x(\mathbf{x}), \quad u_z = w(\mathbf{x}) \tag{1}$$

where $z \in [-t, t]$ defines the thickness coordinate, and where $2t = T$ is the total plate/shell thickness. The definitions of the kinematic variables are depicted on a quadrilateral plate domain in Figure 1. Note that the drilling rotation $\theta_z(\mathbf{x})$ is not part of the plate kinematics; it can, however, be included within interpolation assumptions of the membrane displacements $u(\mathbf{x})$ and $v(\mathbf{x})$, e.g., as described by Cook [58].

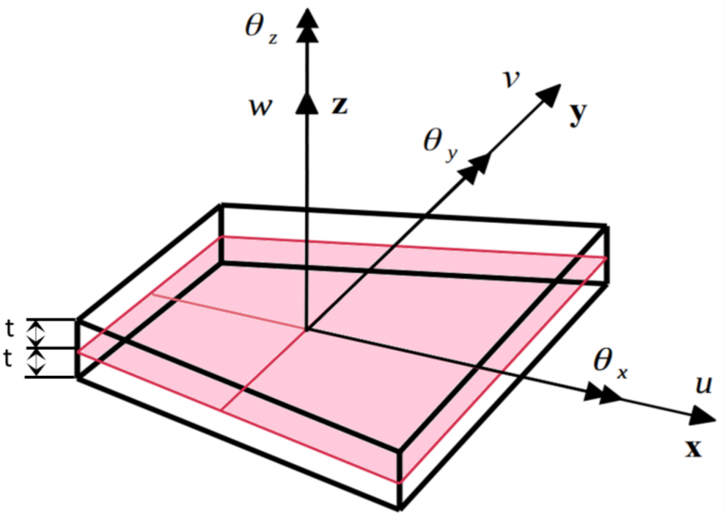

Figure **1**. Notation of Mindlin kinematic variables depicted on a quadrilateral plate.

The infinitesimal in-plane strains are derived from the linear strain-displacement relations of elasticity theory, resulting in

$$\begin{Bmatrix} \varepsilon_{xx} \\ \varepsilon_{yy} \\ \gamma_{xy} \end{Bmatrix} = \begin{Bmatrix} u_{x,x} \\ u_{y,y} \\ u_{x,y} + u_{y,x} \end{Bmatrix} = \mathbf{e} + z\boldsymbol{\kappa} \tag{2}$$

where the three membrane and three curvature section strains are given as

$$\mathbf{e}(u,v) \equiv \begin{Bmatrix} \varepsilon_1 \\ \varepsilon_2 \\ \varepsilon_3 \end{Bmatrix} = \begin{Bmatrix} u_{,x} \\ v_{,y} \\ u_{,y} + v_{,x} \end{Bmatrix}, \ \boldsymbol{\kappa}\left(\theta_x, \theta_y\right) \equiv \begin{Bmatrix} \varepsilon_4 \\ \varepsilon_5 \\ \varepsilon_6 \end{Bmatrix} = \begin{Bmatrix} \theta_{y,x} \\ -\theta_{x,y} \\ -\theta_{x,x} + \theta_{y,y} \end{Bmatrix} \tag{3}$$

The independent assumptions for the deflection, w, and bending rotations, θ_x and θ_y, give rise to the transverse shear strains, given as

$$\mathbf{g}\left(w, \theta_x, \theta_y\right) \equiv \begin{Bmatrix} u_{z,x} + u_{x,z} \\ u_{z,y} + u_{y,z} \end{Bmatrix} = \begin{Bmatrix} w_{,x} + \theta_y \\ w_{,y} - \theta_x \end{Bmatrix} = \begin{Bmatrix} \varepsilon_7 \\ \varepsilon_8 \end{Bmatrix} \tag{4}$$

where $(\bullet)_{,\alpha} \equiv \partial(\bullet)/\partial\alpha$ denotes a partial derivative with respect to the midplane coordinate $(\alpha = x, y)$. Thus, $\mathbf{e}(u,v)$, $\boldsymbol{\kappa}\left(\theta_x, \theta_y\right)$, and $\mathbf{g}\left(w, \theta_x, \theta_y\right)$ are the eight section strain components representing the membrane, bending, and transverse shear section strains.

It is further envisioned that the structure is instrumented with in-situ strain gauges or any type of strain sensors, such as fiber Bragg Grating (FBG) strain sensors or fiber optic strain sensors. These sensors provide real-time strain measurements during structural deformations. The in-situ strain measurements do not provide any information regarding the applied loading on the structure. Figure 2 depicts a typical plate/shell cross-section in the local coordinate frame of reference $\mathbf{x} = (x, y)$ and z. Corresponding to the mid-plane reference position $\mathbf{x}_i = (x, y)_i$, two strain gauges are instrumented at z=*t* and z=−*t*, each providing three strain-component measurements, $\left(\varepsilon_{xx}^{+},\varepsilon_{yy}^{+},\gamma_{xy}^{+}\right)$ at (**x**$_i$, z=*t*) and $\left(\varepsilon_{xx}^{-},\varepsilon_{yy}^{-},\gamma_{xy}^{-}\right)$ at (**x**$_i$, z=−*t*).

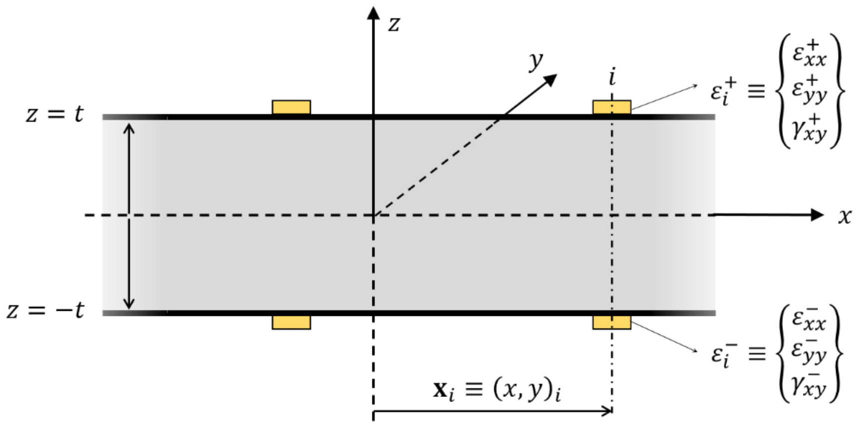

Figure **2**. Plate/shell instrumented with top and bottom strain gauges shown on a cross-section.

Using Eqs. (2), the membrane and curvature section strains due to the strain sensor (strain gauge) measurements at (**x**$_i$, z=*t*) and (**x**$_i$, z=−*t*) can be readily determined at the position **x**$_{\text{i}}$, in as

$$\mathbf{e}_i^{\varepsilon} \equiv \begin{Bmatrix} \varepsilon_1^{\varepsilon} \\ \varepsilon_2^{\varepsilon} \\ \varepsilon_3^{\varepsilon} \end{Bmatrix} = \frac{1}{2}\left(\begin{Bmatrix} \varepsilon_{xx}^{+} \\ \varepsilon_{yy}^{+} \\ \gamma_{xy}^{+} \end{Bmatrix} + \begin{Bmatrix} \varepsilon_{xx}^{-} \\ \varepsilon_{yy}^{-} \\ \gamma_{xy}^{-} \end{Bmatrix}\right) \tag{5.1}$$

$$\boldsymbol{\kappa}_i^{\varepsilon} \equiv \begin{Bmatrix} \varepsilon_4^{\varepsilon} \\ \varepsilon_5^{\varepsilon} \\ \varepsilon_6^{\varepsilon} \end{Bmatrix} = \frac{1}{T}\left(\begin{Bmatrix} \varepsilon_{xx}^{+} \\ \varepsilon_{yy}^{+} \\ \gamma_{xy}^{+} \end{Bmatrix} - \begin{Bmatrix} \varepsilon_{xx}^{-} \\ \varepsilon_{yy}^{-} \\ \gamma_{xy}^{-} \end{Bmatrix}\right) \tag{5.2}$$

where superscript ε signifies that the values are obtained from the actual in-situ strain gauge measurements that may possess random experimental errors.

Within the iFEM formulation, the in-situ experimental section strains, Eqs. (5), and the analytic section strains, Eqs. (3), are required to match in a least-squares sense across the entire iFEM discretization. This is accomplished by a weighted least-squares variational principle, in which these two sets of strains are matched in a least-squares sense for every inverse finite element in the iFEM discretization.

The weighted least-squares element functional, Φ^e, can be expressed as

$$\Phi^e \equiv \boldsymbol{w}_m \, \boldsymbol{\varphi}_m + \boldsymbol{w}_b \, \boldsymbol{\varphi}_b + \boldsymbol{w}_s \, \boldsymbol{\varphi}_s = \sum_{k=1,8} w_k \, \varphi_k \tag{6}$$

where

$$\boldsymbol{w}_m = \begin{bmatrix} w_1 & w_2 & w_3 \end{bmatrix}, \quad \boldsymbol{w}_b = \begin{bmatrix} w_4 & w_5 & w_6 \end{bmatrix}, \quad \boldsymbol{w}_s = \begin{bmatrix} w_7 & w_8 \end{bmatrix}$$

denote the weighting coefficients that enforce either strong or weak correlation between the measured and analytic section strains; the vectors $\boldsymbol{\varphi}_j \; (j = m,b,s)$ are given as the non-dimensional L2 norms

$$\boldsymbol{\varphi}_m \equiv \begin{Bmatrix} \varphi_1 \\ \varphi_2 \\ \varphi_3 \end{Bmatrix} = \frac{1}{A^e} \int_{A^e} \left[\mathbf{e}_i - \mathbf{e}_i^{\varepsilon} \right]^2 d\,A, \quad \boldsymbol{\varphi}_b \equiv \begin{Bmatrix} \varphi_4 \\ \varphi_5 \\ \varphi_6 \end{Bmatrix} = \frac{T^2}{A^e} \int_{A^e} \left[\boldsymbol{\kappa}_i - \boldsymbol{\kappa}_i^{\varepsilon} \right]^2 dA, \quad \boldsymbol{\varphi}_s \equiv \begin{Bmatrix} \varphi_7 \\ \varphi_8 \end{Bmatrix} = \frac{1}{A^e} \int_{A^e} \mathbf{g}^2 dA \tag{7}$$

where A^e denotes the element reference (mid-plane) area. In Eqs. (7), the analytic section strains are evaluated at the locations of the in-situ experimental values computed from Eqs. (5).

The weighting coefficients w_i (i=1−6) are generally set to unity, whereas w_7 and w_8, that are associated with the transverse shear strains, are set to a small value, anywhere in the range of $\lambda = 10^{-6}$–10^{-3}. Note that the transverse shear strains cannot be measured using surface-mounted strain gauges, thus the absence of these strains in Eqs. (7). This weighted strategy allows the enforcement of sufficiently strong correlations between the in-situ (measured) section strains and their corresponding analytic counterparts, whereas the transverse shear strains are represented only by their analytic representations. Moreover, in the event the element is missing a measured section strain component, the corresponding weighting coefficient is set to be small, taking the value of λ. The eight section strains associated with the underlying theory are interrelated by way of four strain compatibility conditions. These strain compatibility conditions are the required integrability conditions leading to a compatible set of the five independent kinematic variables defined in Eq. (1).

The kinematic variables, which appear in Eqs. (1), (6), and (7), can be interpolated with a suitable set of C^0-continuous interpolation functions. Tessler and co-workers [27,59–61] have developed the so-called *anisoparametric* (aka *interdependent*) shape functions that yield highly accurate and robust shear-deformable beam, plate, and shell elements. These functions have also been effectively used for iFEM elements, e.g., in Refs. [26,30]. Herein, we make use of a four-node quadrilateral element iQS4 [28], that was also used in Ref. [49]. This element employs drilling degrees-of-freedom (DOF) for the u and v variables, as in Ref. [58], and uses anisoparametric interpolations developed for a four-node quadrilateral element in Ref. [60]. The iQS4 element has six DOF at each of its four nodes. With the element shape functions defined by the matrix $\mathbf{N}^e$, and the corresponding vector of nodal DOF by the vector $\mathbf{u}^e$, the five kinematic variables are interpolated across the element domain as

$$\begin{bmatrix} u & v & w & \theta_x & \theta_y \end{bmatrix}^T = \mathbf{N}^e \mathbf{u}^e \tag{8}$$

Substituting Eqs. (8) into Eq. (6) and minimizing Φ^e with respect to $\mathbf{u}^e$ results in the element matrix equations of the linear form

$$\mathbf{k}^e \mathbf{u}^e = \mathbf{f}^e \tag{9}$$

where $\mathbf{k}^e$ is a 24×24 symmetric, positive semi-definite matrix of constant coefficients, $\mathbf{u}^e$ is a 24×1 vector of nodal DOF, and $\mathbf{f}^e$ is a 24×1 right-hand vector that is a function of the measured section strains. For the complete details of the matrix equations, the interested reader is referred to [28,49].

The element matrices are assembled using the usual finite element assembly procedure: (1) using appropriate orthogonal transformations, the element matrices are first transformed to correspond to the global DOF, and then (2) assembled into a global system of linear algebraic equations,

$$\mathbf{K}\,\mathbf{U} = \mathbf{F} \tag{10}$$

To solve this system of equations uniquely, the $\mathbf{K}$ matrix must be positive definite. In addition to imposing the requisite displacement boundary conditions that remove rigid-body modes, the iFEM mesh and the corresponding strain sensor distributions must be carefully designed. This latter aspect is of special computational and practical importance.

Considering the cost and practical aspects of installing the strain sensors, the number of strain sensors and their spatial distributions become key considerations. First and foremost, an iFEM mesh and strain sensor locations must be designed to ensure that $\mathbf{K}$ is positive definite. Furthermore, it is desirable to use a relatively fine iFEM mesh to ensure sufficiently accurate predictions of the deformed shape of the structure under consideration.

To facilitate a robust and cost-effective shape-sensing analysis in the presence of relatively few strain sensors, the present paper examines an approach involving two basic analysis steps:

(1) Pre-processing of in-situ (experimental) strain data accomplished by Smoothing Element Analysis (SEA), and

(2) Solving the inverse problem using iFEM that utilizes SEA produced smoothed strain data.

This loosely coupled SEA-iFEM procedure is described in Figure 3. The SEA is a finite element technique that employs a penalized least-squares formulation. The approach treats arbitrarily positioned discrete data of a quantity of interest and outputs a C^1-continuous representation of these data across the entire smoothing domain. The complete mathematical formulation of SEA and the formulations of three- and four-node smoothing elements can be found in the original articles by Tessler and co-authors [51–54]. In the present context, the experimental curvature strain measures (aka section strains) are the quantities to be smoothed by SEA, where each strain measure is smoothed independently. The main appeal of the SEA pre-processing step is that the smoothed strain measures can be output at Gauss integration points corresponding to the iFEM elements, thus allowing a straightforward area integration associated with the terms in Eqs. (7).

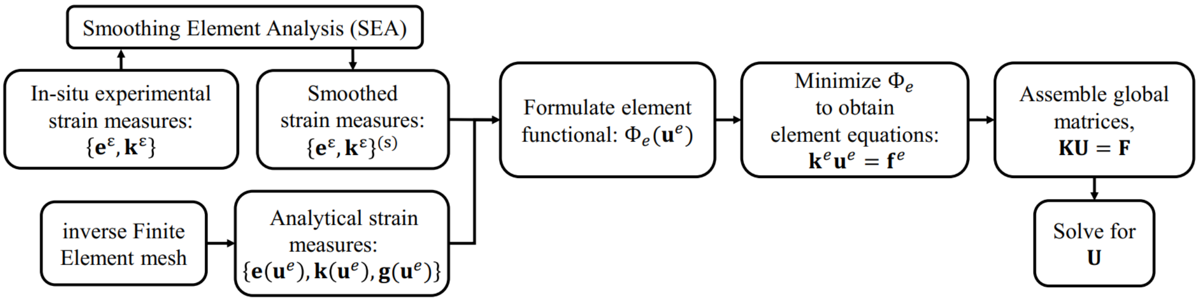

Figure **3**. Flow chart of iFEM procedure aided via pre-processing of in-situ strain data by SEA.

In what follows, a numerical study is presented that is aimed at seeking robust iFEM models using SEA pre-processed experimental strain data. The main objective is to arrive at accurate iFEM predictions when relatively few strain sensors are available.

3. Numerical study

A numerical study is carried out to explore the loosely coupled SEA-iFEM modeling strategy depicted in Figure 3. The key impetus for invoking the SEA pre-processing step is to ensure the robustness of high-fidelity iFEM discretizations in the presence of relatively sparse strain sensor distributions. This framework also allows for a cost-effective design of strain sensor distributions across the structural domain, while keeping the number of sensors to be relatively small. The numerical study attempts to quantify the benefits of the SEA-iFEM modeling by examining relatively simple SEA meshes and their corresponding strain sensors. Such schemes can serve as reference models for more complex structures and applications.

3.1. Problem Definition

As examples of various plate deformation patterns [49], natural vibration modes of a cantilevered rectangular plate are considered to assess the proposed SEA-iFEM shape sensing capability. The plate is made of an aluminium alloy of Young's modulus E $= 73$ GPa, Poisson's ratio $\nu = 0.3$, and density $\rho = 2700$ kg/m^3. The plate dimensions are: span $a = 3$ m, width $b = 1$ m, and thickness $2t$ =1 mm (refer to Figure 4).

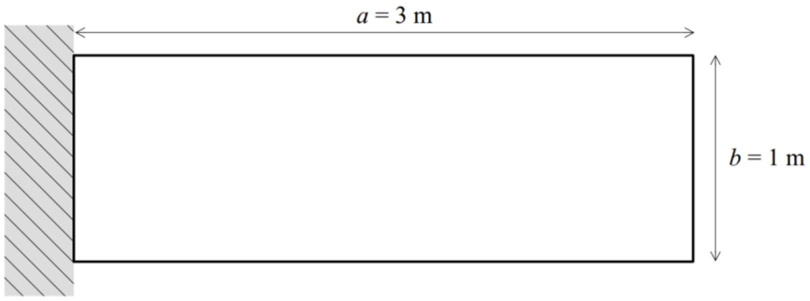

Figure **4**. Cantilevered rectangular plate

Initially, in lieu of an actual experiment, a reference high-fidelity Finite Element Method (FEM) model is developed using the commercial ABAQUS code. The reference FEM model consists of 7550 S4R elements (S4R is a four-node plate element that uses reduced integration of the transverse shear energy.) The strains taken from the reference FEM solutions are regarded as the "experimental" strains, and these are used to calculate the experimental strain measures in Eqs. (5). Furthermore, the nodal displacements of the reference FEM model are used for comparison purposes against those predicted by the iFEM solutions. Since the in-plane strains are anti-symmetric about the midplane, the membrane strain measures, $\mathbf{e}_i^{\varepsilon}$, in Eqs. (5.1) vanish identically. Thus, only single-surface strain sensors (top or bottom) are needed to compute the bending strain measures in accordance with Eqs. (5.2).

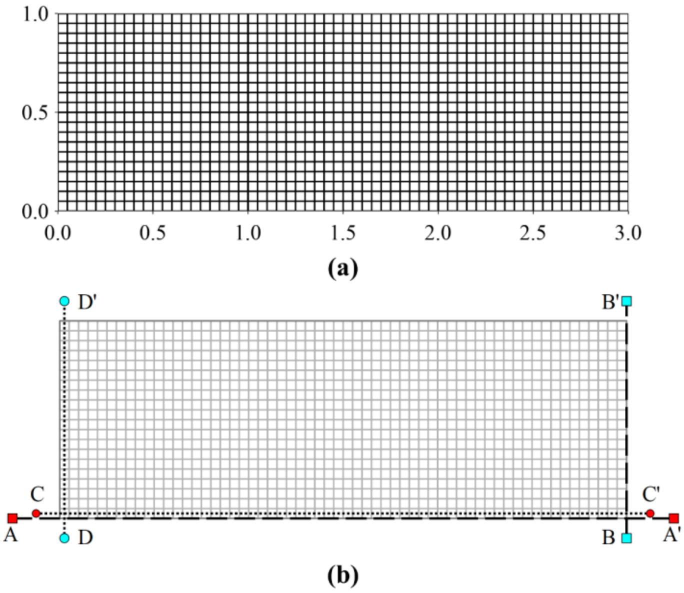

Figure **5**. (**a**) iFEM mesh used, and (**b**) sections where the results are reported.

The iFEM reconstruction is performed using the four-node inverse shell element (iQS4) [28]. The element uses anisoparametric shape functions, where the interpolation of transverse deflection is one order higher than bending rotation to avoid shear locking when enforcing the Kirchhoff constraint. The in-plane and transverse displacement are interpolated bi-quadratically, whereas the bending rotations are interpolated bilinearly. A regular iFEM mesh with a total of 1200 elements is used for the analysis (shown in Figure 5(a)), with 60 elements along the plate length and 20 elements along the plate width. A single strain sensor location is considered per element, with the assumption that the measured strains are constant across the element. The 2×2 Gauss quadrature rule is followed for integrating the error norms of Eq. (7), and the element centroidal strain measure is used at all integration points.

3.2.Baseline iFEM solutions

iFEM reconstruction accuracy solely using high-fidelity FEM strain data is briefly discussed here to establish a set of reference results illustrating the peak iFEM performance that can be developed for a specific problem. The greatest accuracy is expected when all iFEM mesh elements (Figure 5(a)) are instrumented with strain data. This full-field sensor configuration, referred to as ‘CFG-D’, and other efficient sensor patterns (essentially subsets of CFG-D) introduced in Ref. [49], are shown in Figure 6. In this section, iFEM results using CFG-D are presented and will serve as a baseline for all subsequent investigations.

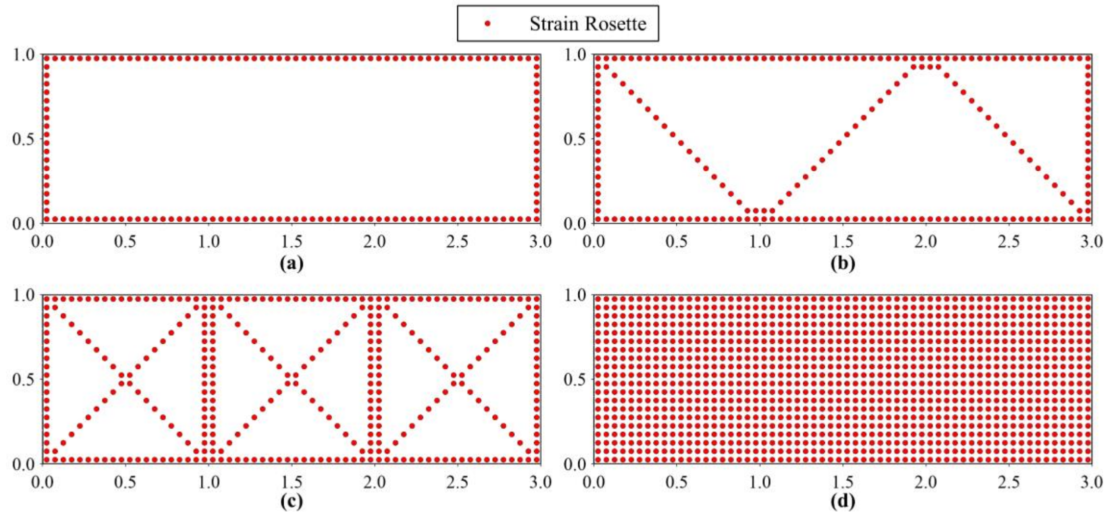

Figure **6**. Sensor configurations: (**a**) CFG-A, (**b**) CFG-B, (**c**) CFG-C, and (**d**) CFG-D

The higher vibrational modes of the plate are considered to assess iFEM results using CFG-D. In particular, the fifth (or second torsional mode) and sixth (or fourth bending mode) modes corresponding to frequencies of 1.84 Hz and 3.27 Hz, respectively, are considered. They present complex plate deformation patterns with symmetric and anti-symmetric deflection distributions. The iFEM reconstructed displacements and rotations are visualized as line plots along the bottom edge (section A-A'), and tip (section B-B') of the plate (refer to Figure 5(b)) and are compared against the reference FEM results. These results are normalized using the maximum value of FEM displacement or rotation along each path.

3.2.1. Baseline results for Mode 5

For the case of Mode 5, the iFEM results for transverse deflection w and rotation θ_x are shown in Figures 7 and 8. These results are highly accurate, with errors of less than 1% along both sections A-A' and B-B'.

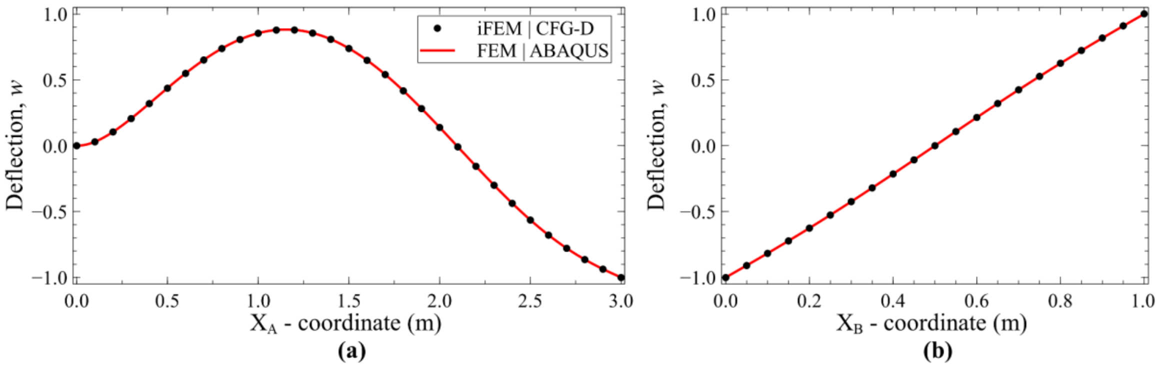

Figure **7**. iFEM reconstructed w for Mode 5 along: (**a**) A-A', and (**b**) B-B'.

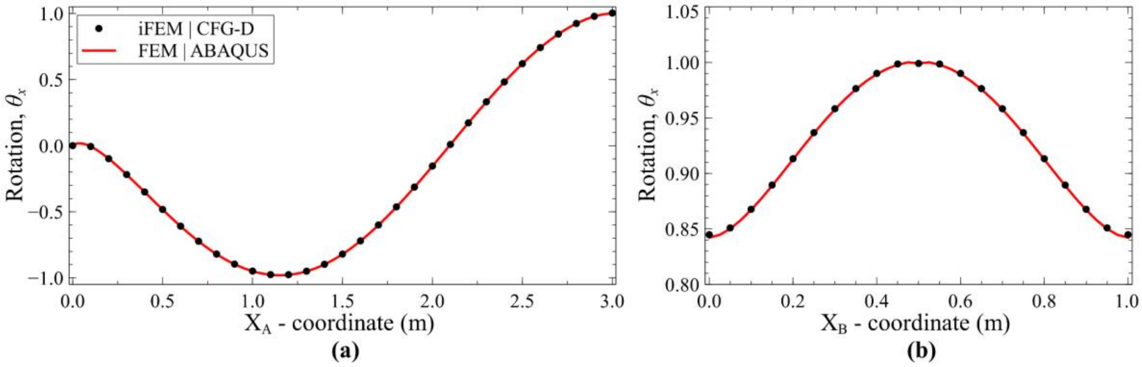

Figure **8**. iFEM reconstructed θ_x for Mode 5 along: (**a**) A-A', and (**b**) B-B'.

The iFEM results for θ_y (shown in Figure 9) also reports an error of less than 1%, illustrating a consistent level of iFEM accuracy for all the deformation components.

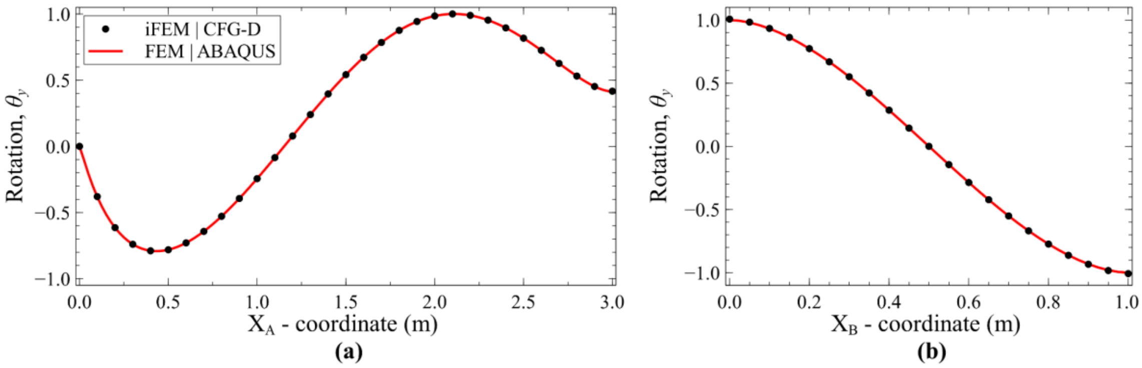

Figure **9**. iFEM reconstructed θ_y for Mode 5 along: (**a**) A-A', and (**b**) B-B'.

3.2.2. Baseline results for Mode 6

The iFEM reconstructed deflection for Mode 6 along A-A' and B-B' is shown in Figure 10.

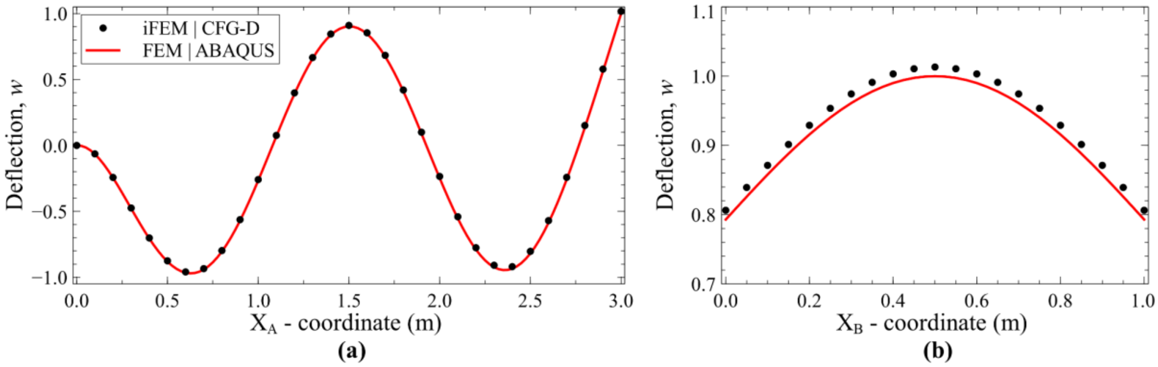

Figure **10**. iFEM reconstructed w for Mode 6 along: (**a**) A-A', and (**b**) B-B'.

The maximum error in w is seen at the plate tip (along B-B'), with a value of ~1.5%. The results for the rotations θ_x and θ_y, shown in Figures 11 and 12, respectively, are similarly accurate with errors less than 1% along both sections.

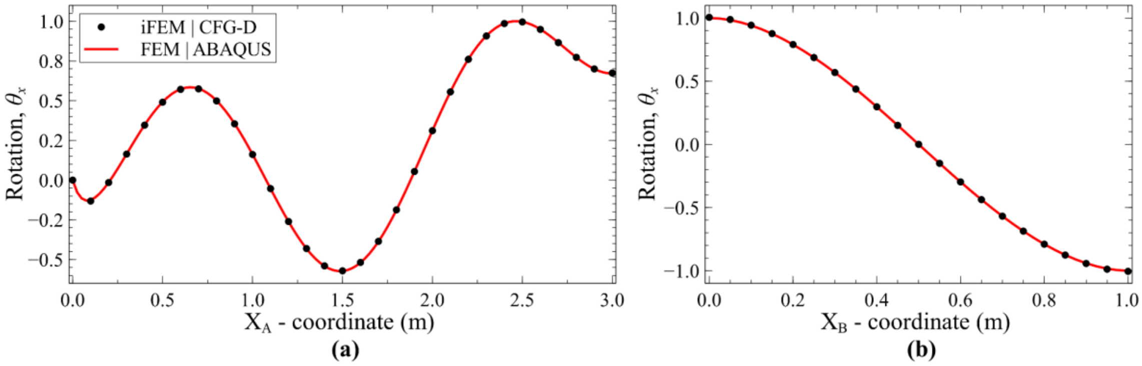

Figure **11**. iFEM reconstructed θ_x for Mode 6 along: (**a**) A-A', and (**b**) B-B'.

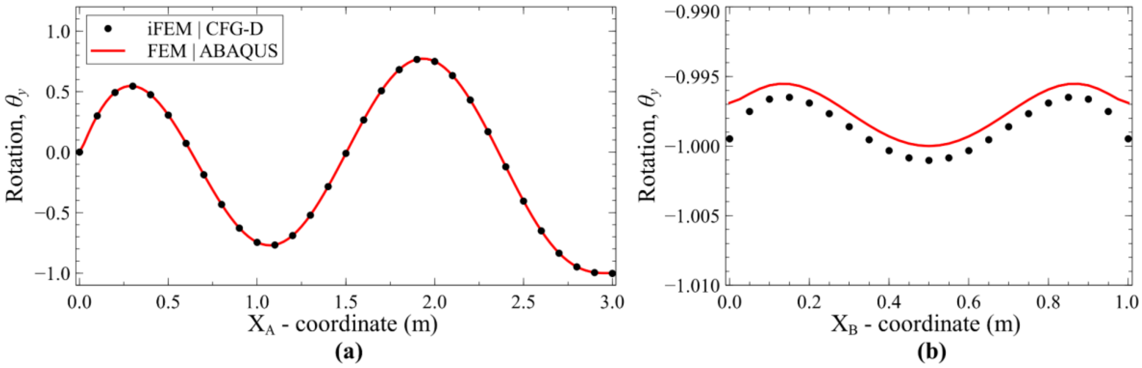

Figure **12**. iFEM reconstructed θ_y for Mode 6 along: (**a**) A-A', and (**b**) B-B'.

The above results demonstrate a baseline iFEM performance with errors ≤~1% when all elements of the iFEM mesh are instrumented with FEM strain data. In the next section relatively sparse strain sensor distributions are introduced, and the use of SEA smoothed strain data as a potential substitute for FEM strain data is investigated.

3.3. Reduced strain sensor patterns

Previous efforts investigating efficient sensor patterns requiring a sparse number of strain sensors identified three viable configurations [49] (see Figure 6): CFG-A (sensors instrumented along the plate boundaries), CFG-B (sensors along plate boundaries and internal zig-zag paths), and CFG-C (sensors along plate boundaries and internal cross-diagonal paths). Among these, CFG-B was deemed an optimal choice as it presented a practical compromise between high reconstruction accuracy and low sensor requirements. CFG-B is characterised by a continuous strain sensor path along the plate boundaries combined with additional sensors along internal zig-zag diagonal paths, ensuring a non-singular and accurate iFEM reconstruction across the plate. It should also be noted that CFG-B uses tri-axial strain measurements (as corresponding to a strain rosette) at each sensor position. The continuity of the sensor pattern is also key to avoid a breakdown of the iFEM procedure due to a singular system matrix.

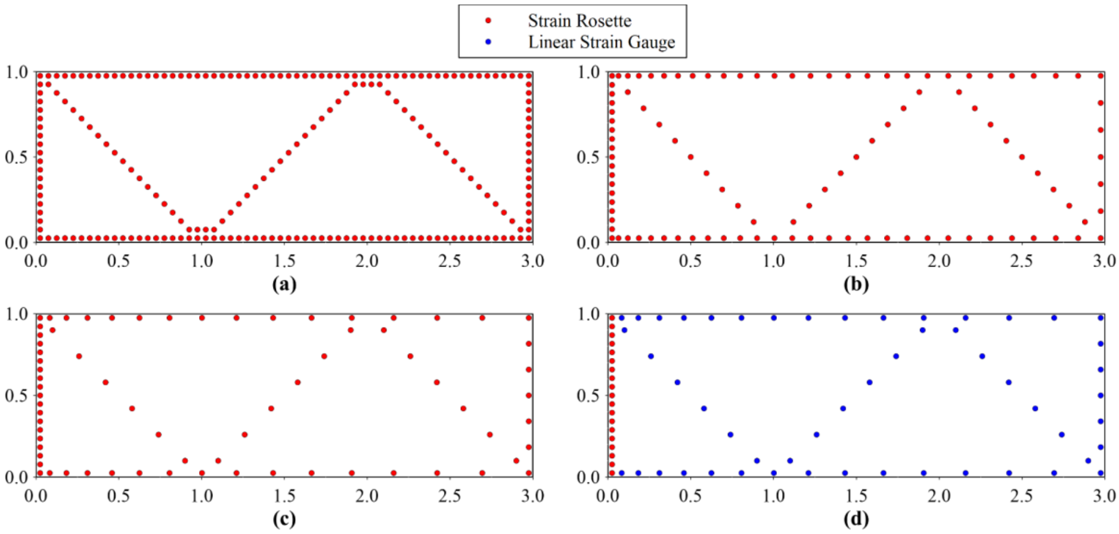

Figure **13**. Strain sensor distributions inspired from CFG-B: (**a**) Full, (**b**) Reduced Set-1 (R1), (**c**) Reduced Set-2 (R2), and (**d**) Reduced Set-3 (R3).

The present study builds on previous results and reduces the number of sensors required by introducing a pre-processing step to smooth the experimental strain data. CFG-B, shown in Figure 13(a), serves as the reference for this study, whereas in Figures 13(b), (c), and (d) are shown three reduced sensor distributions. The R1 example uses a similar sensor configuration to CFG-B, but the number of sensors along each path is significantly reduced. Additionally, the sensor distribution is improved. CFG-B used a uniform distribution of sensors along each sensor path, while in R1, the distribution is skewed such that sensor density is higher close to the clamped edge. This change was inspired by the fact that the root strains have a higher magnitude and a greater influence on the iFEM predictions. R2 further reduces the number of sensors (compared to R1) and incorporates a similar skewed distribution with a higher sensor density close to the clamped end. The R3 pattern is similar to R2, with the only contrasting feature being that tri-axial strain measurements are used only along the clamped end. All other sensor paths, i.e., along the long edges, tip, and internal zig-zag diagonals of the plate, use uni-axial strain measurements (as from a linear strain gauge or fiber optic cable) and signify a substantial reduction in the number of sensors used. These three reduced sensor patterns are the focus of investigation in the following sections.

3.4. Pre-processing of strain data using SEA

The SEA formulation employed in this study is that developed in Ref. [53], where a three-node triangular smoothing element (herein referred to as SEA3) has been developed. The formulation is robust enough to accommodate elements that do not have any in-situ strain data. For each reduced sensor pattern of Section 3.3, SEA models are used to smooth in-situ strain data, where the SEA3 elements are arranged in a cross-diagonal pattern. Independent smoothing meshes are used to smooth strains along each sensor path, as shown in Figure 14. Each smoothing mesh reflects the specific distribution of strain sensors along the path, i.e., along the long edges of the plate, the mesh is progressively finer close to the fixed end (see Figure 14(a)), and along the clamped edge a uniform fine mesh is used (see Figure 14(b)). Also, along the plate tip and internal diagonal paths, uniform meshes are used. In CFG-B, the location of the instrumented strain sensors coincides with each inverse element centroid. However, this is not the case for the reduced sensor patterns; in these new cases, the SEA is used to compute smoothed strains at inverse element centroids corresponding to the boundary and internal elements instrumented in CFG-B.

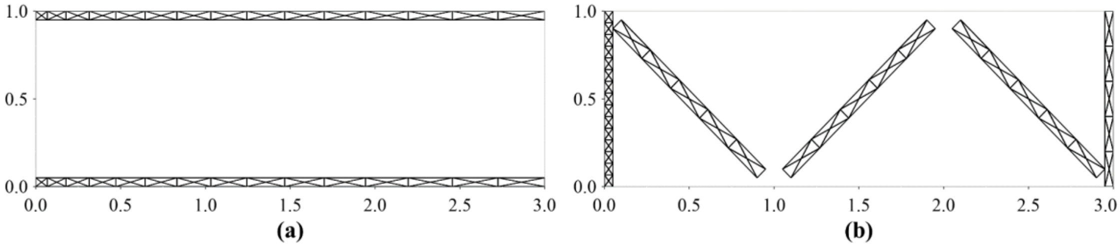

Figure **14**. Smoothing meshes used: (**a**) along the plate length, and (**b**) along the plate width and cross diagonals.

The accuracy of the smoothed strain fields is quantified to assess the feasibility of using smoothed strains as a suitable substitute for in-situ strains at various sensor locations of the plate. The smoothed strains are compared with reference FEM strains along the C−C’ and D−D' sections (refer to Figure 5(b)). All curvature plots are normalized with respect to the maximum FEM curvature along each path.

3.4.1. Results for Mode 5

The SEA smoothed curvatures are depicted in Figures 15-17. Figure 15 shows the results for curvature κ_x along sections C−C' and D−D'. As R2 and R3 have the same sensor distribution along the plate length, the smoothed curvature distribution along C−C' is also similar. The same is applicable for all three sensor patterns along D−D'. Figure 15(a) shows the smoothed κ_x distribution along C−C', where R1 reports a maximum error of 1.12%. The other two patterns are less accurate, with an error of 2.53% close to the plate tip. Along the clamped end, (Figure 15(b)), the smoothed κ_x curvature is highly accurate, with a maximum error of 0.15%.

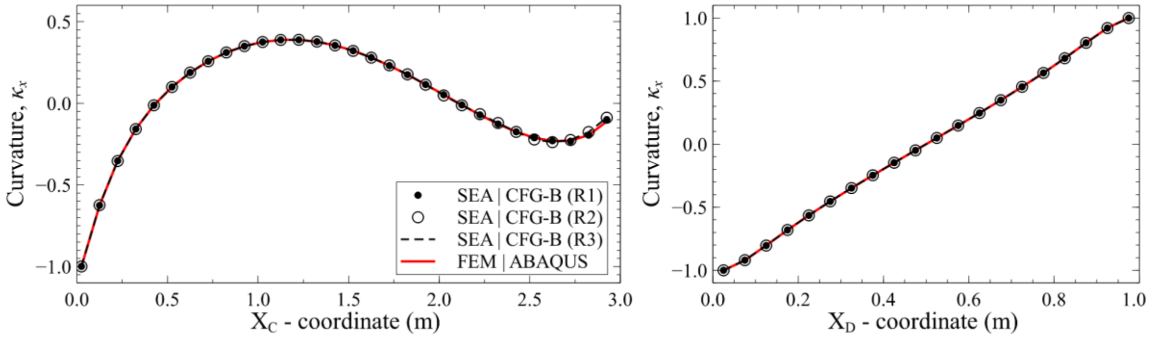

(a) **(b)**

Figure **15**. SEA smoothed κ_x for Mode 5 along: (**a**) C−C', and (**b**) D−D'.

Given that Mode 5 is a torsional mode, all three curvature components are equally important for displacement reconstruction. However, accurate smoothing of κ_{xy} and κ_y involves difficulties due to their complex variation along the clamped end of the plate. Figures 16(b) and 17(b) shows the plots of curvatures, κ_{xy} and κ_y along section D−D', where it is evident that only a high order polynomial expansion can capture such a complex variation. As the C^1-continuous strain field produced by the SEA is dependent on the smoothing mesh used, a dense mesh is required along the clamped end to smooth the root curvatures accurately. The smoothing mesh used along the clamped end is shown in Figure 14(b). It should be noted that as only ε_{xx} strain measurements are available for R3 along C−C', curvatures κ_{xy} and κ_y are unavailable and cannot be smoothed along this section. Smoothing results for κ_{xy} along C−C' are very accurate with a maximum error of less than 1.2% for R1 and R2. Along D−D', the results are similar for all three cases, where the maximum error is close to 5.2% at the corners. Smoothing results for κ_y along C−C' are less accurate with a maximum error of 4.3% for R1 and 8.52% for R2, reported close to the plate tip. Along the clamped end, a maximum error of 4.5% is observed.

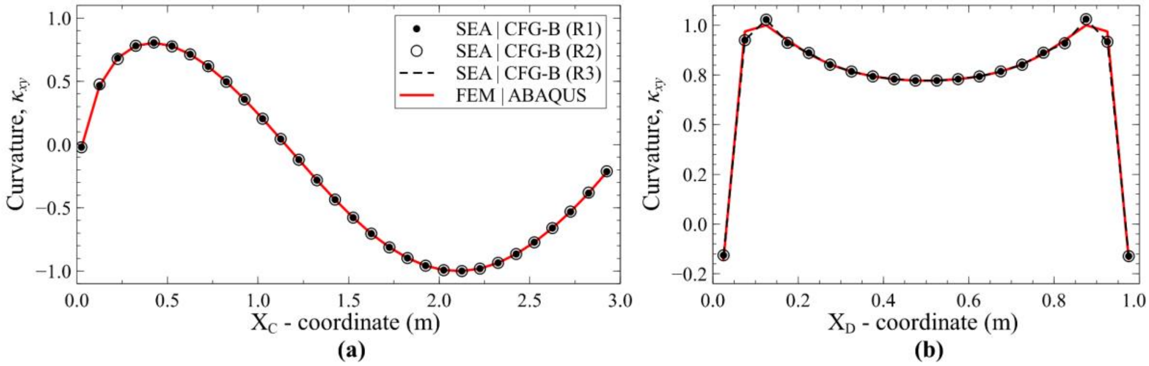

(a) (b)

Figure **16**. SEA smoothed κ_{xy} for Mode 5 along: (**a**) C−C', and (**b**) D−D'.

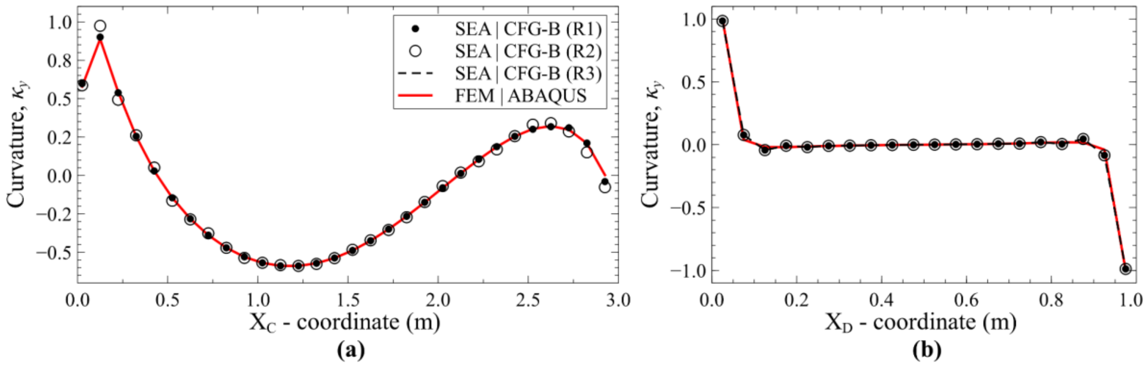

(a) (b)

Figure **17**. SEA smoothed κ_y for Mode 5 along: (**a**) C−C', and (**b**) D−D'.

The smoothed curvature plots of Figures 16 and 17 verify that the refined smoothing mesh is capable of accurately smoothing the curvature distribution along the clamped end. Errors in the smoothed curvatures are observed near the plate corners, i.e., the top and bottom corners of the clamped end. These errors indicate that SEA is unable to recreate localised high-order curvature variations. Also, curvature κ_y results along C−C' (Figure 17(a)) demonstrates that R1 is more accurate, especially close to the plate tip, compared to R2 and R3 due to the greater sensor density near the tip. Overall, the smoothing results for Mode 5 are sufficiently accurate. Next, these smoothed strains are used for the iFEM analysis, and the reconstruction results are shown in a later section.

3.4.2. Results for Mode 6

In Mode 6 the κ_x curvature has a higher magnitude and a greater influence over the displacement field than κ_{xy} and κ_y. Hence, there is a greater emphasis on accurately smoothing curvature κ_x. The curvature distribution along path C−C' is composed of multiple peaks, following the various nodes and antinodes of the displacement field. The curvature distribution along D−D' is similar to that in Mode 5, where the variation can be modelled using a high-order polynomial. Overall, Mode 6 presents an excellent test case in smoothing a complex curvature field. Smoothing results for κ_x along C−C' are shown in Figure 18(a), and it reports a maximum error of ~1% for R1 and ~4% for the other two sets, with the major inaccuracies occurring close to the plate tip. It can be seen from Figure 18(b) that results along D−D' is very accurate with a maximum error of less than 0.15%.

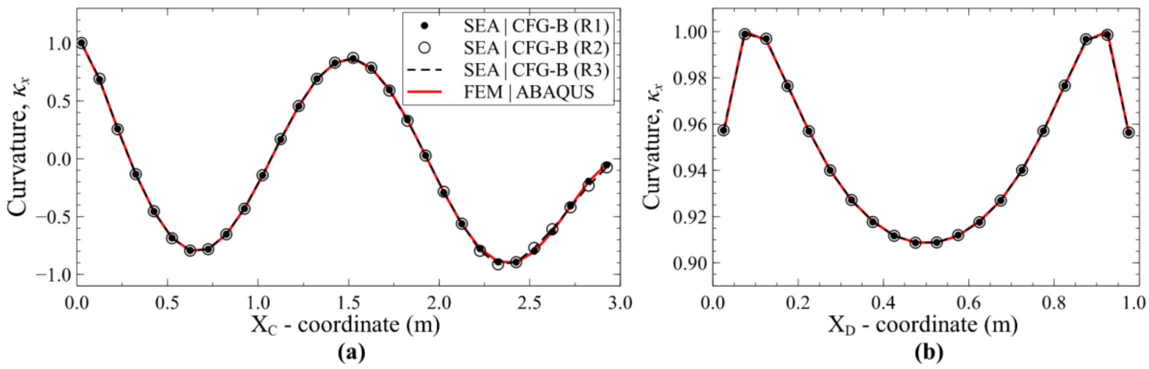

(a)
(b)

Figure **18**. SEA smoothed κ_x for Mode 6 along: (**a**) C−C', and (**b**) D−D'.

The smoothed curvature distributions along the path C−C' are very accurate with minor errors in curvature κ_x toward the plate tip ($X_C = 3$ m). These inaccuracies could result from the coarse sensor distribution and coarse smoothing mesh used near the plate tip. However, as the magnitude of the curvatures is lower near the tip, these errors are not expected to contribute to a significant degradation in the displacement reconstruction accuracy. Compared to Mode 5, the more complex nature of the curvature field along the path C−C' (with multiple peaks) should be noted, and the results reported here are encouraging. SEA results for κ_{xy} and κ_y are shown in Figures 19 and 20, respectively. Along C−C', the maximum error in κ_{xy} is less than 1.6%, while along D−D' it is ~3.6%. Similar, but slightly less accurate results are observed for κ_y ; a maximum error of 1.8% and 5.9% for R1 and R2, respectively, along C−C', and 4% along D−D'.

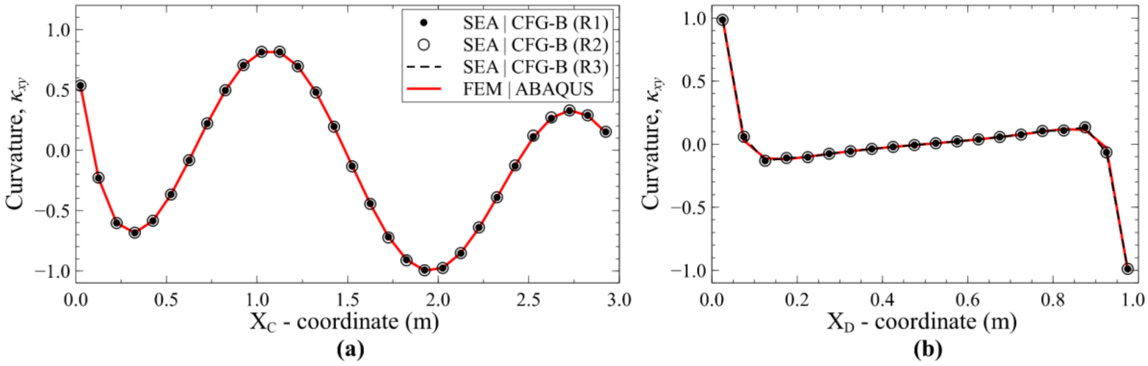

Figure **19**. SEA smoothed κ_{xy} for Mode 6 along: (**a**) C−C', and (**b**) D−D'.

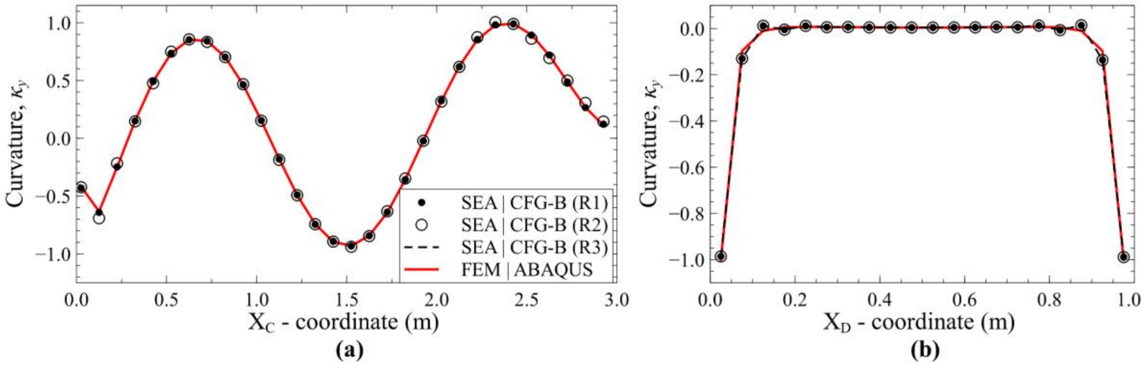

Figure **20**. SEA smoothed κ_y for Mode 6 along: (**a**) C−C', and (**b**) D−D'.

Along the clamped end, SEA performance was similar to that observed for Mode 5. Due to the complex nature of the curvature distribution, localized errors are observed close to the upper and lower corners of the plate, as seen in Figures 19(b) and 20(b). Here, a more refined smoothing mesh near the plate corners might lead to a more accurate smoothing of the curvature field. Overall, the relatively simple SEA models produced sufficiently accurate strain results for application within the iFEM analysis.

3.5. iFEM reconstruction using smoothed strain data

The SEA smoothed curvatures are used as experimental strain data for the iFEM analysis. As previously stated, for each reduced sensor pattern (R1, R2, or R3), smoothed curvatures are extracted at element centroids corresponding to the instrumented strain sensor positions of CFG-B. Thus, iFEM analysis using CFG-B will use in-situ strain data at all relevant element centroids, while iFEM analysis using R1, R2, and R3 will use smoothed strain data at the same element centroidal positions. Although the number of in-situ strain sensor locations are different for each case, the same number of smoothed strain data locations are used as input for the iFEM analysis. A total of 214 smoothed strain data points are used, corresponding to the centroids of 214 elements. For elements with no strain data, the weighting coefficients of Eq. (6) are set to a small value, i.e., 10^{-4}. Similarly, as the transverse shear strains cannot be measured using surface mounted strain sensors, the corresponding weighting coefficients (w_7 and w_8) are also set to be small for all elements. The analysis cases are summarized in Table 1. The iFEM results based on SEA smoothed strain data are referred to as iFEM$^{(s)}$.

Table **1**. Labels, sensor, and mesh details of the various reduced sensor sets explored in the present study.

Analysis Type	**Strain sensor Configuration (CFG)**	**Sensor Set**	**No. of in-situ Strain Sensor Locations**	**No. of iFEM Input Strain Data Locations**	**Element and Mesh Information**	
					Element Type	**No. of Elements**
FEM | ABAQUS	--	--	--	--	S4R	7,550

iFEM | CFG-B	CFG-B	Full	214	214	iQS4	1,200
iFEM$^{(S)}$ | CFG-B (R1)	CFG-B	Reduced 1 (R1)	107	214	SEA3 | iQS4	260 | 1,200
iFEM$^{(S)}$ | CFG-B (R2)	CFG-B	Reduced 2 (R2)	72	214	SEA3 | iQS4	260 | 1,200
iFEM$^{(S)}$ | CFG-B (R3)	CFG-B	Reduced 3 (R3)	72	214	SEA3 | iQS4	260 | 1,200

The iFEM results are presented as line plots of the reconstructed transverse deflection, w, and rotations, θ_x and θ_y at nodes along the plate length (section A−A') and along the plate tip (section B−B'). Figure 5(b) shows the various sections used for reporting the results. As the maximum transverse deflection in the case of Mode 5 occurs along the plate tip, considering section B−B' is of importance. The iFEM results presented in this section are normalised using the maximum magnitude of FEM deflection or rotation along each path. Additionally, contour plots of the deflections and rotations are also provided to illustrate the spatial distribution of the various deformation variables.

3.5.1. Results for Mode 5

The iFEM reconstructed deflection w for Mode 5 along sections A−A' and B−B' are shown in Figure 21. The deflection results along both paths are highly accurate, with the maximum error not exceeding 1% along A−A', and less than 2.4% along B−B' for all three reduced sensor patterns.

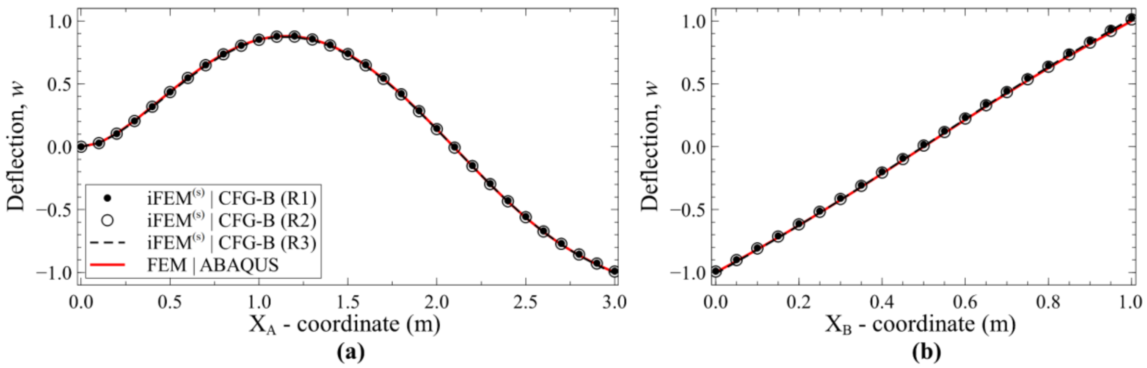

Figure **21**. iFEM reconstructed w for Mode 5 along: (**a**) A−A', and (**b**) B−B'.

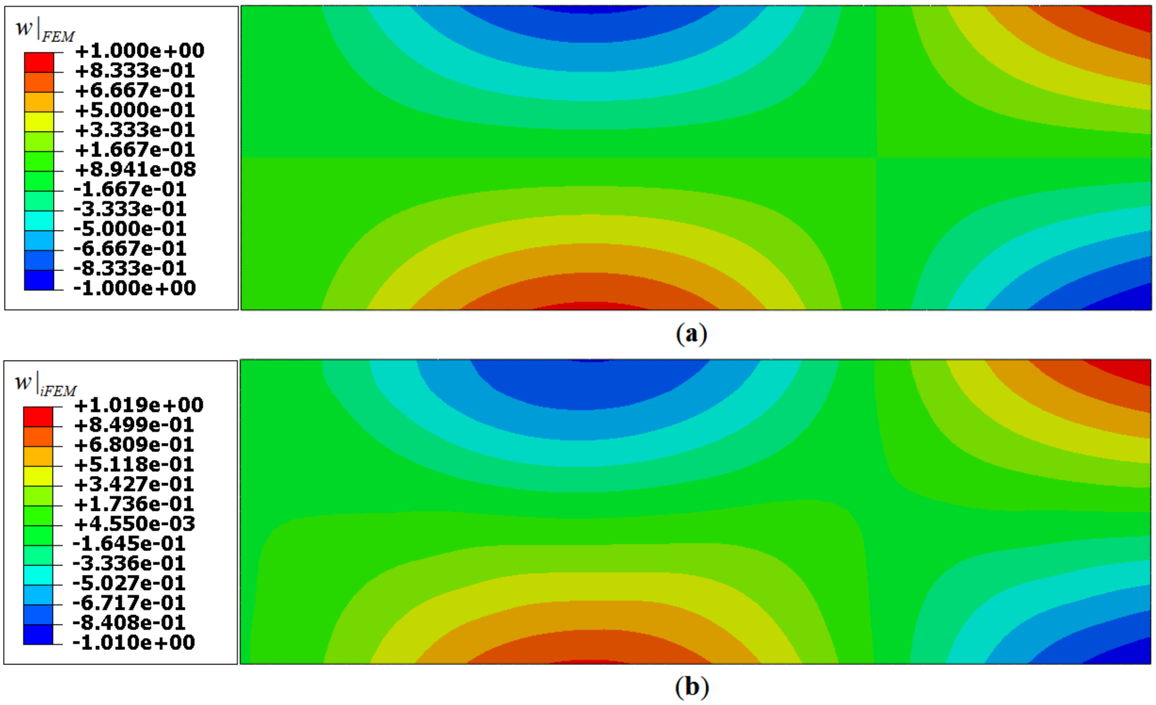

Figure **22**. Contour plot of w for Mode 5: (**a**) FEM, and (**b**) R3 results

A contour plot of the iFEM results is also presented to highlight the spatial variation of the reconstructed displacements and rotations. Figure 22 shows contour plots comparing the FEM and iFEM transverse deflection fields. Among the reduced sensor patterns investigated, R3 is expected to be the limiting case, producing the least accurate results due to the extremely low quantity of in-situ strain sensors used. Hence, iFEM results for R3 are shown in Figure 22(b). No significant difference is observed from a cursory visual inspection of the two contour plots. Comparing maximum deflection magnitudes from both plots reveals a tip deflection error of 1.9%, reinforcing the conclusions derived from Figure 21(b).

The iFEM reconstruction results for θ_x along A−A' and B−B' are shown in Figure 23. In contrast to the transverse deflection results, the θ_x results present significant differences among the three sensor patterns. Results for R1 and R2 are similar and accurate, with a maximum error of less than 1.5% along both the sections. However, R3 results are different, with a maximum error of ~3.5% along the tip and ~13.7% along the plate length. The poor accuracy of R3 is further evident from the contour plots of θ_x shown in Figure 24.

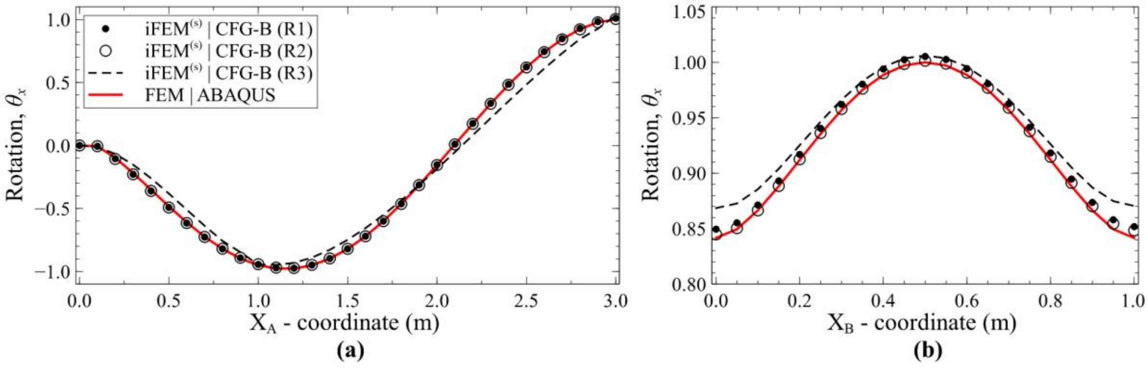

Figure **23**. iFEM reconstructed θ_x for Mode 5 along: (**a**) A−A', and (**b**) B−B'.

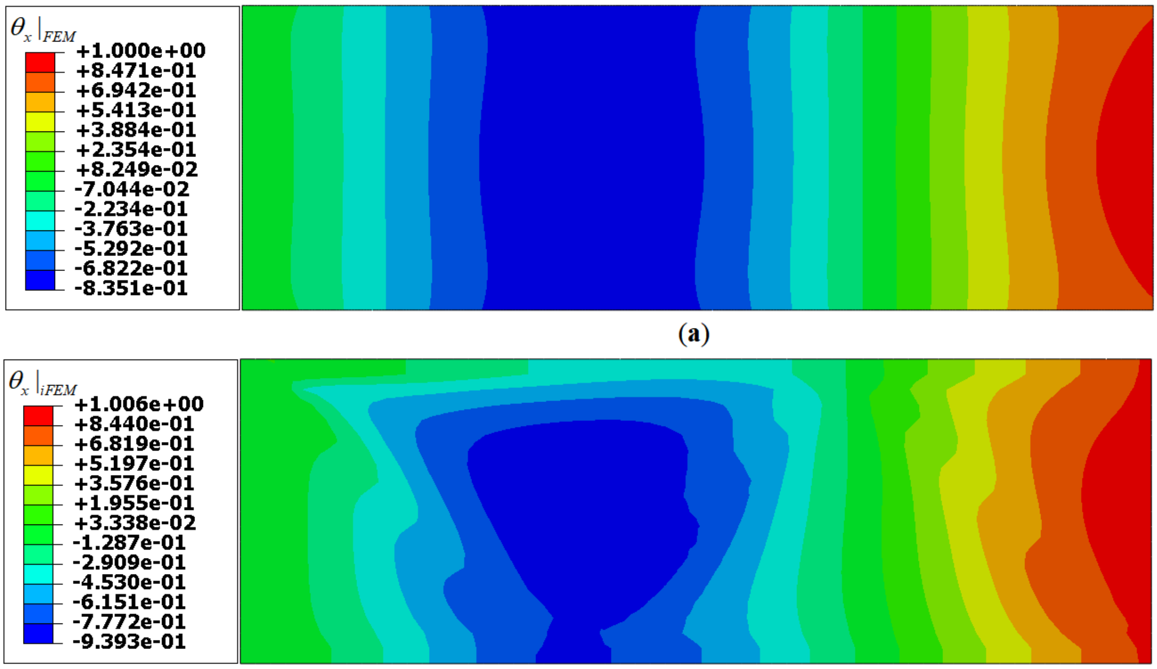

(a)

(b)

Figure **24**. Contour plot of θ_x for Mode 5: (**a**) FEM, and (**b**) R3 results

Decline in R3 accuracy is attributed to the lack in quantity and quality of curvature data available for the iFEM procedure. As R3 utilizes tri-axial strain data only along the clamped end, all other sensor paths lack information regarding either one or two curvature components; κ_y and κ_{xy} data is unavailable along the plate length, while κ_x and κ_{xy} data is unavailable along the plate tip. This substantial lack of curvature data at internal locations of the plate can even lead to a breakdown of the iFEM procedure. This deficit is resolved to a certain extent using strain data along the zig-zag paths. This curvature component, oriented along the plate diagonal and referred to as $\kappa_{x,45}$, is a mixture of κ_x, κ_y and κ_{xy}. Using $\kappa_{x,45}$ and the boundary curvatures, iFEM attempts to recreate a continuous deformation field. However, the lack of curvature data is a hindrance to the iFEM procedure leading to reconstruction errors observed at internal nodes of the plate.

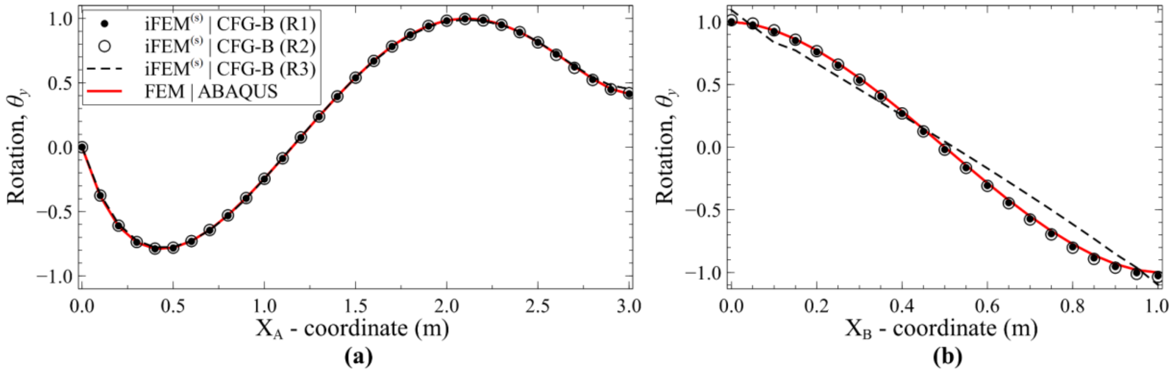

Figure **25**. iFEM reconstructed θ_y for Mode 5 along: (**a**) A−A', and (**b**) B−B'.

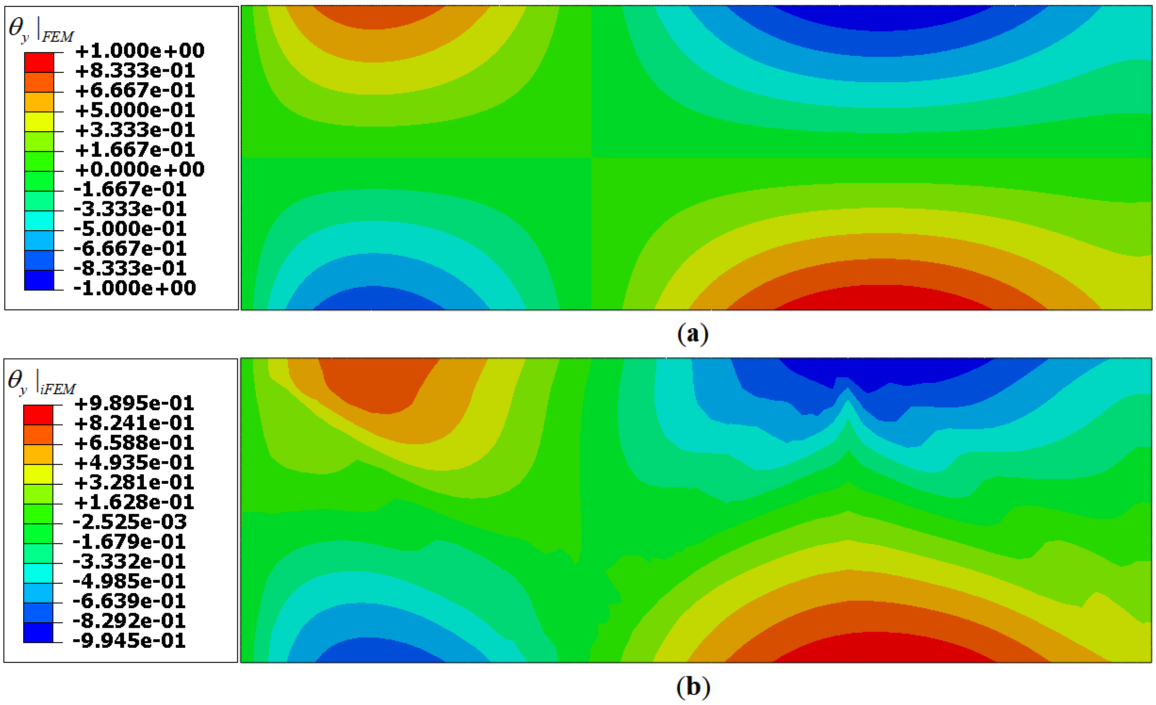

Figure **26**. Contour plot of θ_y for Mode 5: (**a**) FEM, and (**b**) R3 results

The reconstruction results for θ_y along A−A' and B−B' are shown in Figure 25. The plots are similar to those observed for θ_x i.e., results along the plate length are accurate for all three cases, with a maximum error of 1% for R1 and R2 and ~4% for R3. However, results along the plate tip reveals inaccuracies; R1 and R2 reports a maximum error of ~3.5 %, while R3 produces errors as high as 17 %. It should be noted that the magnitude of θ_y along the tip is small, which might have contributed to some of the errors observed. The contour plots of θ_y (shown in Figure 26) give a clearer picture of the inaccuracies at internal nodes of the plate. Although θ_y is accurate at the plate boundaries, errors are observed further inwards. Similar to the previous case, these errors are attributed to the lack of internal curvature data.

Among the three reduced sensor patterns investigated, iFEM reconstruction results for R1 and R2 are observed to be very accurate. For the case of R3, although deflection results are accurate, rotation reconstruction revealed significant errors. But these conclusions should be put in perspective considering the extremely sparse set of strain data used for R3. Another observation is the high reconstruction accuracy along paths instrumented with strain sensors. A similar conclusion was also stated in Ref. [49]. The results for Mode 6 are analysed in the next section.

3.5.2. Results for Mode 6

This section presents the iFEM results using SEA smoothed curvatures for Mode 6. The iFEM reconstructed deflections along paths $A-A'$ and $B-B'$ are shown in Figure 27. Similar to Mode 5, the deflection results along both paths are highly accurate, with a maximum error less than 2.5 % along the plate length, and less than 2% along the plate tip.

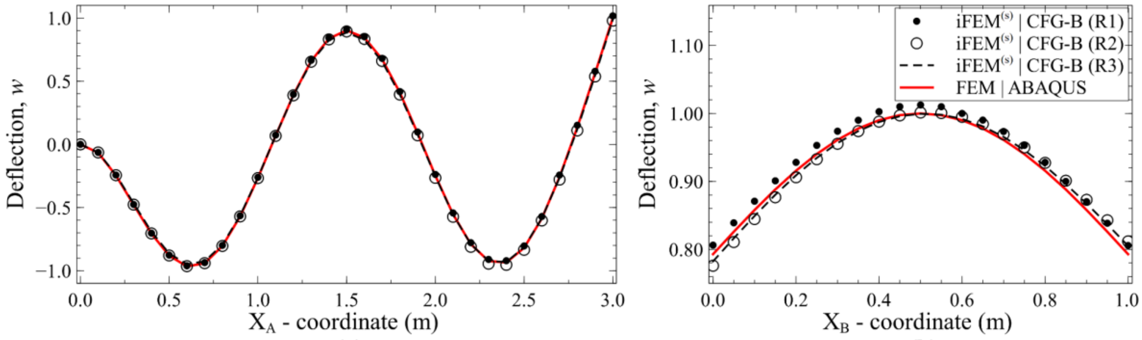

(a) **(b)**

Figure **27**. iFEM reconstructed w for Mode 6 along: (**a**) A−A', and (**b**) B−B'.

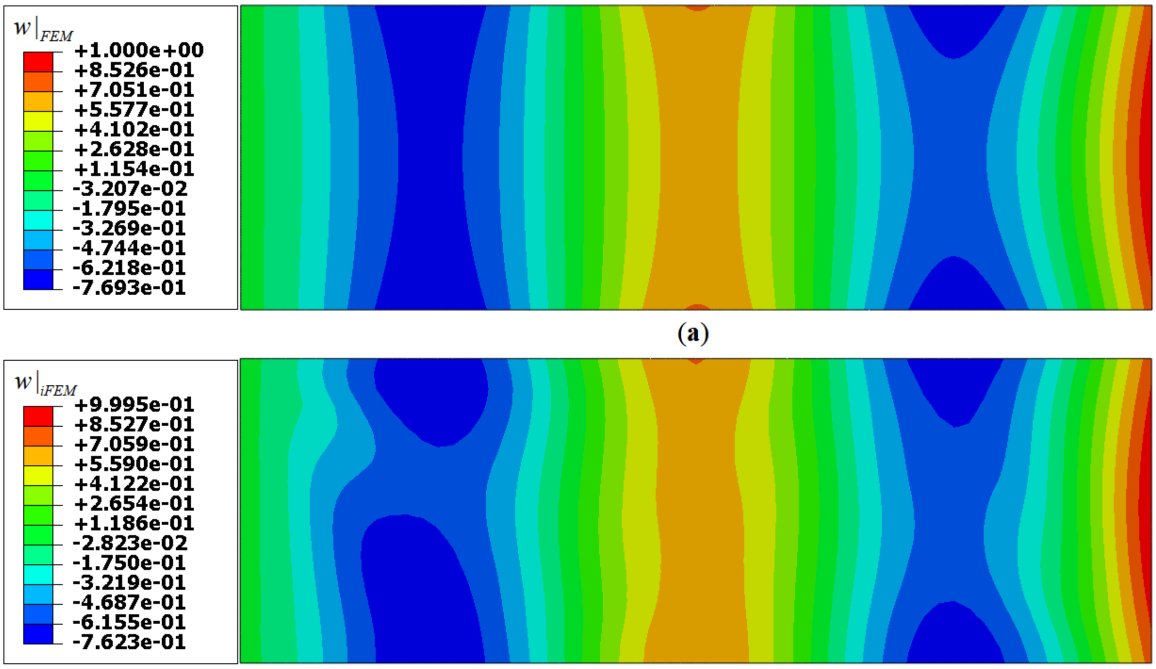

(a)

(b)

Figure **28**. Contour plot of w for Mode 6: (**a**) FEM, and (**b**) R3 results.

An interesting aspect of these results for R2 and R3 is the asymmetry along the plate tip, as seen in Figure 27(b). This is attributed to the use of an asymmetric sensor pattern combined with the sparse nature of the sensor distribution. However, the asymmetry observed is small and not overly concerning. The contour plot of the deflection field, shown in Figure 28, reveals further errors in the case of R3 at internal plate nodes. These results are less accurate than those of Mode 5 and the cause is again attributed to the lack of tri-axial curvature data available for iFEM reconstruction.

The iFEM results for θ_x along A−A' and B−B' are shown in Figure 29. Results along A−A' reveal diminishing levels of accuracy, with a maximum error of 3.7%, 7.5%, and 48.5% for R1, R2, and R3, respectively (see Figure 29(a)). The low magnitude of θ_x for Mode 6 (which is a bending mode), combined with the absence of κ_y curvature data along the plate length results in a relatively poor reconstruction of θ_x along A−A'. However, as κ_y information is available along the plate tip, θ_x reconstruction is more accurate along B−B', with errors on the order of 0.5% for R1 and less than 6.5% for R2 and R3. These results again highlight the high reconstruction accuracy observed along the paths instrumented with sensors.

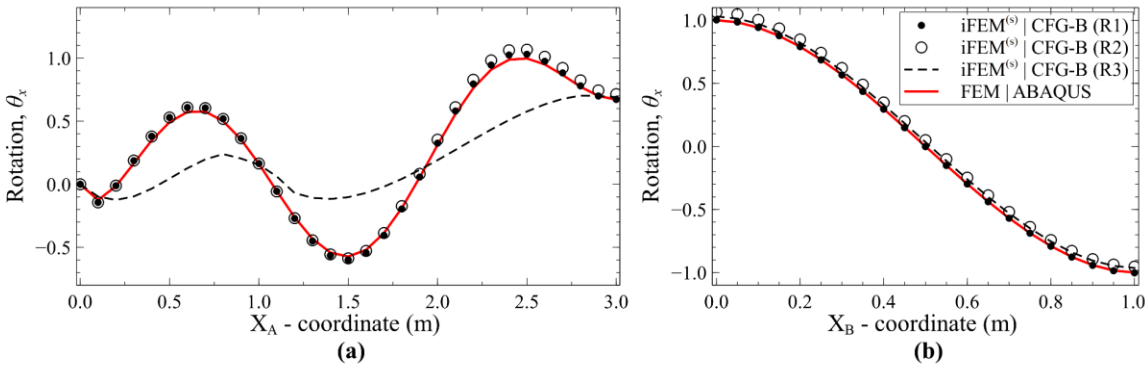

Figure **29**. iFEM reconstructed θ_x for Mode 6 along: (**a**) A−A', and (**b**) B−B'.

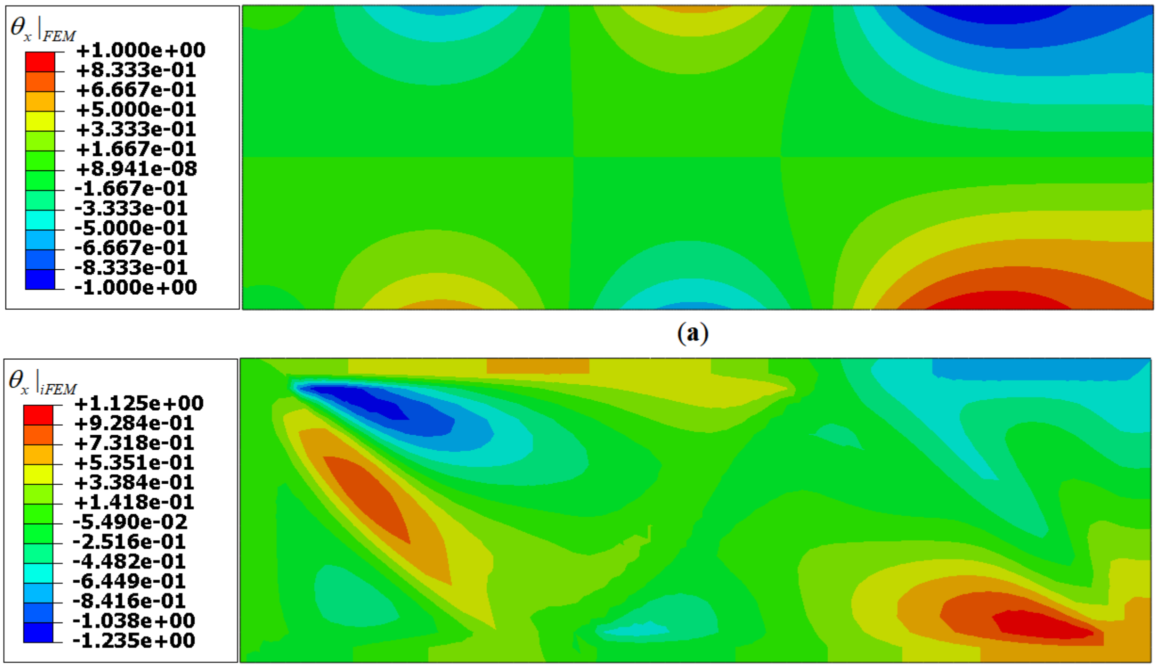

(a)

(b)

Figure **30**. Contour plot of θ_x for Mode 6: (**a**) FEM, and (**b**) R3 results

The contour plots of θ_x are shown in Figure 30, and they highlight the errors already discussed in the results of R3. The reconstructed rotation θ_y along paths, A−A' and B−B' are shown in Figure 31. The reconstruction results along both paths are seen to be very accurate, with the maximum of less than 2% along both sections. Since for this mode, θ_y is the dominant rotation, accurate smoothing of the corresponding curvature κ_x is important. Sufficient information regarding this curvature component is available due to the straight strain sensor paths along the top and bottom edges of the plate, available in all three reduced sensor sets, leading to an accurate rotation reconstruction.

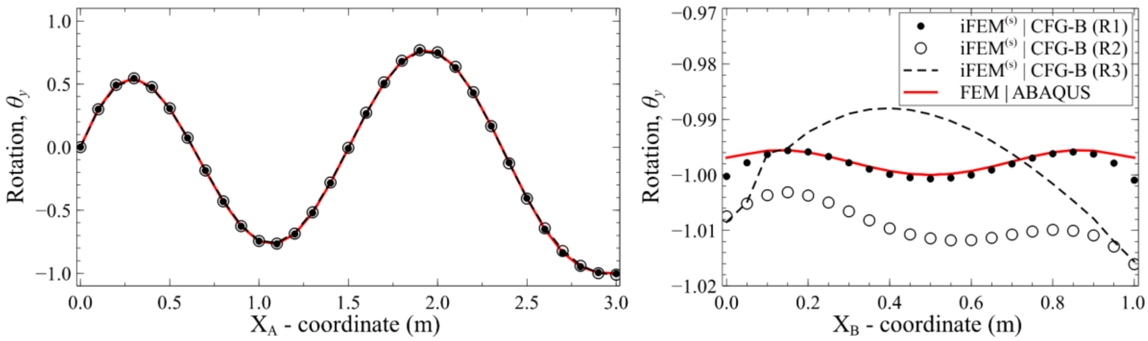

(a) **(b)**

Figure **31**. iFEM reconstructed θ_y for Mode 6 along: (**a**) A−A', and (**b**) B−B’.

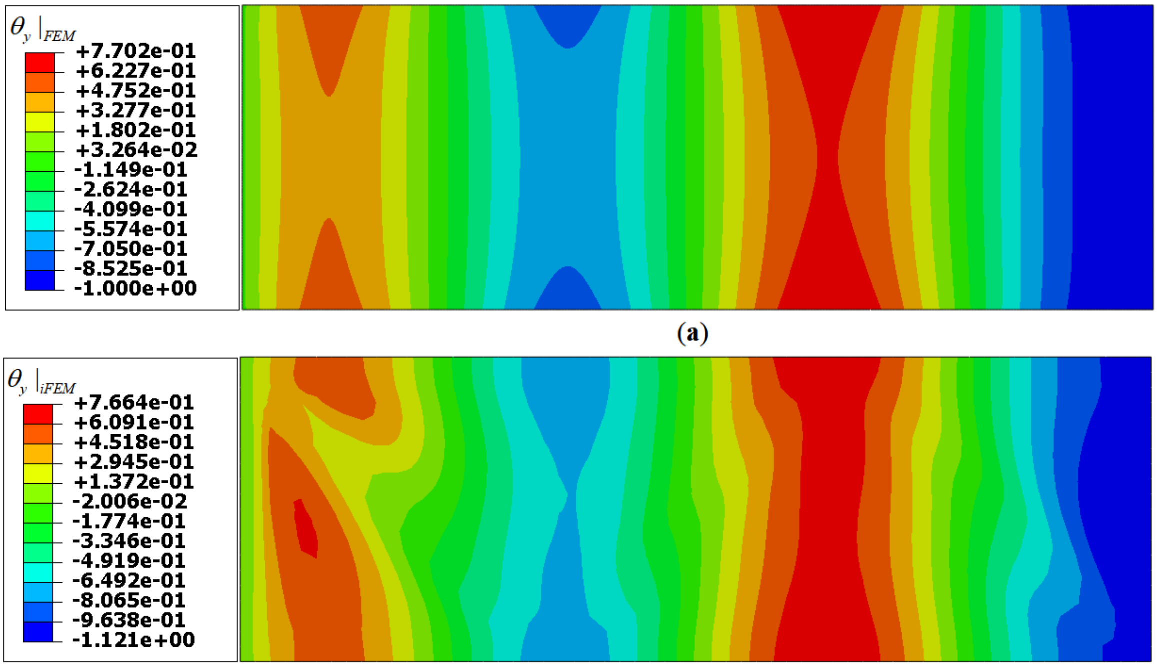

(a)

(b)

Figure **32**. Contour plot of θ_y for Mode 6: (**a**) FEM, and (**b**) R3 results.

The contour plots of θ_y, shown in Figure 32, reveals errors in the results of R3. Although rotation reconstruction along sensor paths are seen to be accurate, it did not lead to an accurate reconstruction at internal nodes of the plate.

It can be concluded from the iFEM results that sensor patterns R1 and R2 are accurate in reconstructing the deflection and rotation fields corresponding to the fifth and sixth vibration modes of the plate. R3 produced good results for deflection, but rotation reconstruction is poor due to the lack of curvature data available. However, these results should be contrasted against the number, location, and nature of strain sensor data used for each case. Although R1 and R2 produced accurate results, they require 107 and 72 strain rosettes, respectively, which is relatively high. In contrast, R3 requires only 19 strain rosettes and a single fiber optic cable, which is highly appealing from a practical point-of-view. Additionally, the use of fiber optic sensors affords the possibility of extracting significantly more uni-axial strain data due to its high measurement density. Such an increase in available strain data could lead to an improvement in the iFEM results as well.

The main drawback of R3 is the lack of curvature data along the internal zig-zag paths of the plate. The curvature measured along the diagonal paths is not sufficient for iFEM to generate an accurate interpolation of the bending rotation between the κ_x data along the plate length and κ_y data along the plate tip. A better alternative is to use cross-diagonal sensor patterns (CFG-C in Figure 6). However, this strategy is accompanied by a corresponding increase in the number of strain sensors required. Regardless, these results successfully demonstrated the effectiveness of using smoothed strain data as a viable alternative to in-situ strain measurements, thus reducing the number of strain sensors required for practical shape sensing applications.

3.6. Root Mean Square error of iFEM results

Herein, we compute the Root Mean Square (RMS) error, e_{RMS}, of the reconstructed displacement field to quantify the reconstruction accuracy over the entire plate domain. For each reduced sensor pattern, the RMS error in the nodal deflection and rotation fields of Modes 5 and 6 are estimated as,

$$e_{RMS}\left(p\right)=\sqrt{\sum_{i=1}^{N_{nod}}\frac{1}{N_{nod}}\left(\frac{p_i^{FEM}-p_i^{iFEM}}{p^{FEM}\left.\right|_{\max}}\right)^2}\times 100\ ,\quad p\in\left\{w,\theta_x,\theta_y\right\} \tag{11}$$

where N_{nod} is the total number of nodes of the iFEM mesh. The error is plotted against the number of uniaxial strain measurements, n_{uni} (or number of linear strain gauges) used for each sensor pattern. This choice of plot is inspired by the need to include the results of R3, which is primarily constituted of uniaxial strain measurements along the plate length and tip. The RMS error of iFEM|CFG-B and -D are also computed to serve as reference values in comparison with the reduced sensor patterns. The variation of e_{RMS} for transverse deflection w and rotation θ_x as a function of sensor quantity is shown in Figure 33.

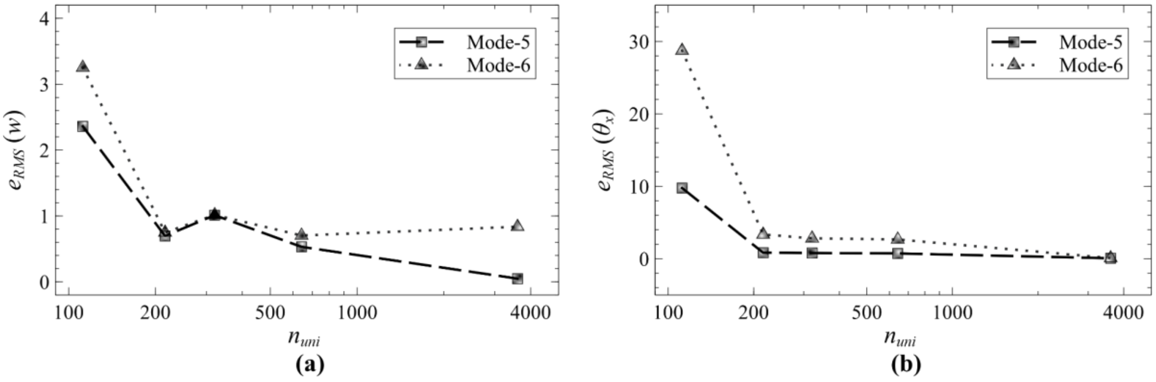

Figure **33**. Variation of e_{RMS} as a function of n_{uni} for: (**a**) w, and (**b**) θ_x

The results show that e_{RMS} reduces with increase in the number of sensors used. The plot of Figure 33(a) shows a maximum error of 3.5%, highlighting the high reconstruction accuracy of transverse deflection across all sensor patterns. In Figure 33(b), the highest error was observed for R3, further illustrating the inaccuracy in reconstructing θ_x. Aside from R3, the errors of R1 and R2 converge quickly to those of the reference sensor patterns.

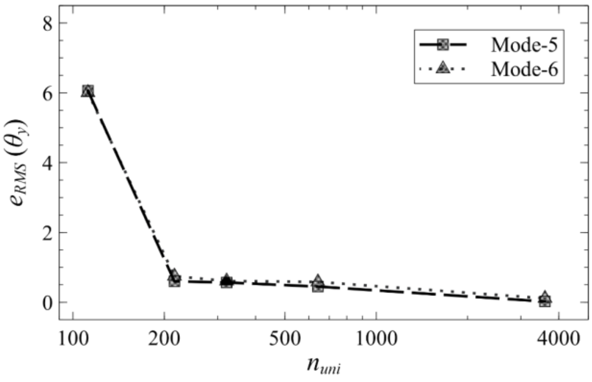

Figure **34**. Variation of e_{RMS} as a function of n_{uni} for θ_y

The error plot for θ_y is shown in Figure 34, with e_{RMS} displaying a similar decreasing trend as a function of n_{uni}. However, the magnitude of the errors is not as high as that observed in Figure 33(b). An explanation for this behaviour is that the majority of strain sensors in R3 are oriented along the plate length, which aids in θ_y reconstruction but not in θ_x reconstruction.

These results further reinforce the conclusions derived in Sections 3.5 by providing a more global perspective of iFEM results across the entire plate. The high accuracy of the reduced sensor patterns in reconstructing transverse deflection has been further demonstrated.

3.7. Influence of Measurement Noise

This section investigates the effect of measurement noise on the reconstruction accuracy of the coupled SEA-iFEM approach. The problem of reconstructing Mode 6 using R1 is investigated again, but now the in-situ strains are contaminated with different levels of measurement noise. The noise is introduced as a percentage of the strain magnitude and follows a Gaussian distribution with zero mean and the value of three standard deviations ranging from 2.5% and 7.5%.

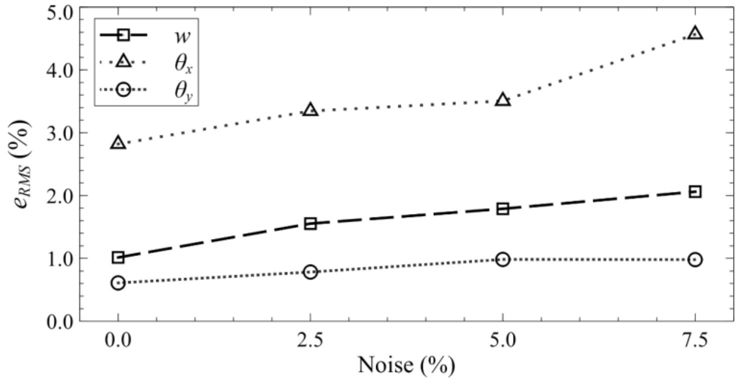

Figure **35**. Change in RMS error of as a function of measurement noise for Mode 6

The results of this study are shown in Figure 35, where the RMS error in reconstructed deflection and rotations (computed using Eq. (11)) are plotted as a function of the noise level. As expected, the results show an increase in error with greater levels of noise, however, the magnitude of increase is not substantial. Every 2.5% level increase in noise level only led to a <1% increase in RMS error for all the kinematic variables. In addition to the accuracy, these results display the robustness of the coupled SEA-iFEM approach.

4. Conclusions

The inverse problem of reconstructing structural deformations based on measured strain data, i.e., shape sensing, was demonstrated in the study of an aluminium plate undergoing complex bending and twisting deformations. The critical focus was to examine whether stable and accurate solutions can be obtained when the structure is instrumented with only a relatively small number of surface-mounted strain gauges or fibre-optic strain sensors. A high-fidelity finite element solution was used as the experimental testbed for the strain gauge data retrieval and displacement field assessment.

Within this computational study, high-fidelity iFEM models were used for solving the inverse reconstruction problem. As a pre-processing step to iFEM, suitable SEA models were developed to smooth the in-situ strain sensor data and to generate additional strain data to be seeded into a high-fidelity iFEM discretization. This modeling strategy allows stable and accurate solutions to be obtained even when many inverse elements do not possess any strain measurements. Several novel strategies were examined for effective utilization of this loosely coupled SEA - iFEM approach. To simulate strain data acquired from fiber-optic strain sensing networks, positions of strain sensors are assumed to be distributed along fiber-optic lines. To pre-process the in-situ strain data, SEA models were used along the strain-data directions. The resulting smoothed strains, that are practically C^1 continuous, were then mapped onto the high-fidelity iFEM discretizations. This novel SEA-iFEM modeling approach demonstrates that even with a relatively small number of strain sensors and judicial choice of strain sensor layouts, accurate plate and shell shape-sensing reconstructions can be obtained. The methodology has beneficial implications for practical industrial applications in structural health monitoring.

Declaration of Funding Sources

This research did not receive any specific grant from funding agencies in the public, commercial, or not-for-profit sectors.

Declaration of Competing Interest

The authors declare that they have no known competing financial interests or personal relationships that could have appeared to influence the work reported in this paper

References

1. Benedettini, O.; Baines, T.S.; Lightfoot, H.W.; Greenough, R.M. State-of-the-art in integrated vehicle health management. *Proc. Inst. Mech. Eng. Part G J. Aerosp. Eng.* **2009**, *223*, 157–170, doi:10.1243/09544100JAERO446.

2. Baroth, E.; Powers, W.T.; Fox, J.; Prosser, B.; Pallix, J.; Schweikard, K.; Zakrajsek, J. IVHM (Integrated Vehicle Health Management) techniques for future space vehicles. *37th Jt. Propuls. Conf. Exhib.* **2001**, doi:10.2514/6.2001-3523.

3. Esperon-Miguez, M.; John, P.; Jennions, I.K. A review of Integrated Vehicle Health Management tools for legacy platforms: Challenges and opportunities. *Prog. Aerosp. Sci.* **2013**, *56*, 19–34, doi:10.1016/j.paerosci.2012.04.003.

4. Agathos, K.; Chatzi, E.; Bordas, S.P.A. Multiple crack detection in 3D using a stable XFEM and global optimization. *Comput. Mech.* **2018**, *62*, 835–852, doi:10.1007/s00466-017-1532-y.

5. Agathos, K.; Tatsis, K.; Nicoli, S.; Bordas, S.P.A.; Chatzi, E. Crack detection in Mindlin-Reissner plates under dynamic loads based on fusion of data and models. *Comput. Struct.* **2021**, *246*, 106475, doi:10.1016/j.compstruc.2020.106475.

6. Butler, T.; Jakeman, J.; Wildey, T. Combining push-forward measures and bayes' rule to construct consistent solutions to stochastic inverse problems. **2018**, *40*, 984–1011.

7. Spiridonakos, M.D.; Chatzi, E.N. Metamodeling of dynamic nonlinear structural

systems through polynomial chaos NARX models. *Comput. Struct.* **2015**, *157*, 99–113, doi:10.1016/j.compstruc.2015.05.002.

8. Moës, N.; Dolbow, J.; Belytschko, T. A finite element method for crack growth without remeshing. *Int. J. Numer. Methods Eng.* **1999**, *46*, 131–150, doi:10.1002/(SICI)1097-0207(19990910)46:1<131::AID-NME726>3.0.CO;2-J.
9. Deshpande, S.; Lengiewicz, J.; Bordas, S.P.A. FEM-based Real-Time Simulations of Large Deformations with Probabilistic Deep Learning. *arXiv* **2021**, doi:10.48550/ARXIV.2111.01867.
10. Prosser, W.H.; Allison, S.G.; Woodard, S.E.; Wincheski, R.A.; Cooper, E.G.; Price, D.C.; Hedley, M.; Prokopenko, M.; Scott, D.A.; Tessler, A. Structural health management for future aerospace vehicles. *Proc. 2nd Australas. Work. Struct. Heal. Monit. Melbourne, Aust.* **2004**, 1–8.
11. Valasek, J. *Morphing Aerospace Vehicles and Structures*; John Wiley & Sons: West Sussex, PO19 8SQ, United Kingdom, 2012; ISBN 9780470972861.
12. Sofla, A.Y.N.; Meguid, S.A.; Tan, K.T.; Yeo, W.K. Shape morphing of aircraft wing: Status and challenges. *Mater. Des.* **2010**, *31*, 1284–1292, doi:10.1016/j.matdes.2009.09.011.
13. McGowan, A.-M.R.; Washburn, A.E.; Horta, L.G.; Bryant, R.G.; Cox, D.E.; Siochi, E.J.; Padula, S.L.; Holloway, N.M. Recent Results from NASA’s Morphing Project [C]. *SPIE’s 9th Annu. Int. Symp. Smart Struct. Mater.* **2002**, *4698*, 97–111.
14. Akl, W.; Poh, S.; Baz, A. Wireless and distributed sensing of the shape of morphing structures. *Sensors Actuators, A Phys.* **2007**, *140*, 94–102, doi:10.1016/j.sna.2007.06.026.

15. Smoker, J.; Baz, A. Monitoring the bending and twist of morphing structures. *Sensors Smart Struct. Technol. Civil, Mech. Aerosp. Syst.* **2008**, *6932*, 69321X, doi:10.1117/12.776433.

16. Gherlone, M.; Cerracchio, P.; Mattone, M. Shape sensing methods: Review and experimental comparison on a wing-shaped plate. *Prog. Aerosp. Sci.* **2018**, *99*, 14–26, doi:10.1016/j.paerosci.2018.04.001.

17. Bruno, R.; Toomarian, N.; Salama, M. Shape estimation from incomplete measurements: A neural-net approach. *Smart Mater. Struct.* **1994**, *3*, 92–97, doi:10.1088/0964-1726/3/2/002.

18. Foss, G.C.; Haugse, E. Using modal test results to develop strain to displacement transformations. In Proceedings of the 13th International Modal Analysis Conference; Nashville, 1995.

19. Lively, P.S.; Atalla, M.J.; Hagood, N.W. Investigation of filtering techniques applied to the dynamic shape estimation problem. *Smart Mater. Struct.* **2001**, *10*, 264–272, doi:10.1088/0964-1726/10/2/311.

20. Bogert, P.B.; Haugse, E.; Works, B.P.; Gehrki, R.E.; Martin, L. Structural shape identification from experimental strains using a modal transformation technique. *Proc. 44th AIAA/ASME/ASCE/AHS Struct. Struct. Dyn. Mater. Conf.* **2003**, 1–18.

21. Kim, N.S.; Cho, N.S. Estimating deflection of a simple beam model using fiber optic Bragg-grating sensors. *Exp. Mech.* **2004**, *44*, 433–439, doi:10.1177/0014485104045431.

22. Tessler, A.; Spangler, J.L. A Variational Principle for Reconstruction of Elastic Deformations in Shear Deformable Plates and Shells. *NASA/TM-2003-212445* 2003.

23. Tessler, A.; Spangler, J.L. A least-squares variational method for full-field reconstruction of elastic deformations in shear-deformable plates and shells. *Comput. Methods Appl. Mech. Eng.* **2005**, *194*, 327–339, doi:10.1016/j.cma.2004.03.015.

24. Ko, W.L.; Richards, W.L.; Tran, V.T. Displacement Theories for In-Flight Deformed Shape Predictions of Aerospace Structures. *NASA/TP-2007-214612* 2007.

25. Ko, W.L.; Richards, W.L.; Fleischer, V.T. Applications of Ko Displacement Theory to the Deformed Shape Predictions of the Doubly-tapered Ikhana Wing. *NASA/TP-2009-214652.* 2009.

26. Tessler, A.; Spangler, J. Inverse FEM for Full-Field Reconstruction of Elastic Deformations in Shear Deformable Plates and Shells. *Proc. Second Eur. Work. Struct. Heal. Monit.* **2004**, 83–90.

27. Tessler, A.; Hughes, T.J.R. A three-node mindlin plate element with improved transverse shear. *Comput. Methods Appl. Mech. Eng.* **1985**, *50*, 71–101, doi:10.1016/0045-7825(85)90114-8.

28. Kefal, A.; Oterkus, E.; Tessler, A.; Spangler, J.L. A quadrilateral inverse-shell element with drilling degrees of freedom for shape sensing and structural health monitoring. *Eng. Sci. Technol. an Int. J.* **2016**, *19*, 1299–1313, doi:10.1016/j.jestch.2016.03.006.

29. Kefal, A. An efficient curved inverse-shell element for shape sensing and structural health monitoring of cylindrical marine structures. *Ocean Eng.* **2019**, *188*, 106262, doi:10.1016/j.oceaneng.2019.106262.

30. Gherlone, M.; Cerracchio, P.; Mattone, M.; Di Sciuva, M.; Tessler, A. Shape sensing of 3D frame structures using an inverse Finite Element Method. *Int. J. Solids Struct.* **2012**, *49*, 3100–3112, doi:10.1016/j.ijsolstr.2012.06.009.

31. Roy, R.; Gherlone, M.; Surace, C. A shape sensing methodology for beams with generic cross-sections: Application to airfoil beams. *Aerosp. Sci. Technol.* **2021**, *110,* 106484, doi:10.1016/j.ast.2020.106484.

32. Cerracchio, P.; Gherlone, M.; Tessler, A. Real-time displacement monitoring of a composite stiffened panel subjected to mechanical and thermal loads. *Meccanica* **2015**, *50,* 2487–2496, doi:10.1007/s11012-015-0146-8.

33. Esposito, M.; Gherlone, M. Composite wing box deformed-shape reconstruction based on measured strains: Optimization and comparison of existing approaches. *Aerosp. Sci. Technol.* **2020**, *99*, 105758, doi:10.1016/j.ast.2020.105758.

34. Esposito, M.; Gherlone, M. Material and strain sensing uncertainties quantification for the shape sensing of a composite wing box. *Mech. Syst. Signal Process.* **2021**, *160,* 107875, doi:10.1016/j.ymssp.2021.107875.

35. Kefal, A.; Oterkus, E. Displacement and stress monitoring of a Panamax containership using inverse finite element method. *Ocean Eng.* **2016**, *119*, 16–29, doi:10.1016/j.oceaneng.2016.04.025.

36. Kefal, A.; Mayang, J.B.; Oterkus, E.; Yildiz, M. Three dimensional shape and stress monitoring of bulk carriers based on iFEM methodology. *Ocean Eng.* **2018**, *147*, 256–267, doi:10.1016/j.oceaneng.2017.10.040.

37. Colombo, L.; Sbarufatti, C.; Giglio, M. Definition of a load adaptive baseline by inverse finite element method for structural damage identification. *Mech. Syst. Signal Process.* **2019**, *120,* 584–607, doi:10.1016/j.ymssp.2018.10.041.

38. Roy, R.; Gherlone, M.; Surace, C. *Damage Localisation in Thin Plates Using the Inverse Finite Element Method*; Springer Singapore, 2020; Vol. 2; ISBN

9789811383304.

39. Roy, R.; Gherlone, M.; Surace, C.; Tessler, A. Full-Field Strain Reconstruction Using Uniaxial Strain Measurements: Application to Damage Detection. *Appl. Sci.* **2021**, *11*, 1681, doi:10.3390/app11041681.

40. Li, M.; Kefal, A.; Cerik, B.C.; Oterkus, E. Dent damage identification in stiffened cylindrical structures using inverse Finite Element Method. *Ocean Eng.* **2020**, *198*, 106944, doi:10.1016/j.oceaneng.2020.106944.

41. Li, M.; Kefal, A.; Oterkus, E.; Oterkus, S. Structural health monitoring of an offshore wind turbine tower using iFEM methodology. *Ocean Eng.* **2020**, *204*, 107291, doi:10.1016/j.oceaneng.2020.107291.

42. Miller, E.J.; Manalo, R.; Tessler, A. Full-Field Reconstruction of Structural Deformations and Loads from Measured Strain Data on a Wing Test Article using the Inverse Finite Element Method. *NASA/TM—2016–219407* **2016**.

43. Kefal, A.; Tabrizi, I.E.; Tansan, M.; Kisa, E.; Yildiz, M. An experimental implementation of inverse finite element method for real-time shape and strain sensing of composite and sandwich structures. *Compos. Struct.* **2021**, *258*, 113431, doi:10.1016/j.compstruct.2020.113431.

44. Oboe, D.; Colombo, L.; Sbarufatti, C.; Giglio, M. Shape Sensing of a Complex Aeronautical Structure with Inverse Finite Element Method. *Sensors* **2021**, *21*, 1388, doi:https://doi.org/10.3390/s21041388.

45. Colombo, L.; Oboe, D.; Sbarufatti, C.; Cadini, F.; Russo, S.; Giglio, M. Shape sensing and damage identification with iFEM on a composite structure subjected to impact damage and non-trivial boundary conditions. *Mech. Syst. Signal Process.* **2021**, *148*,

107163, doi:10.1016/j.ymssp.2020.107163.

46. Kefal, A.; Yildiz, M. Modeling of sensor placement strategy for shape sensing and structural health monitoring of a wing-shaped sandwich panel using inverse finite element method. *Sensors (Switzerland)* **2017**, *17*, doi:10.3390/s17122775.

47. Zhao, Y.; Du, J.; Bao, H.; Xu, Q. Optimal Sensor Placement for Inverse Finite Element Reconstruction of Three-Dimensional Frame Deformation. *Int. J. Aerosp. Eng.* **2018**, *2018*, doi:10.1155/2018/6121293.

48. Zhao, Y.; Du, J.; Bao, H.; Xu, Q. Optimal sensor placement based on eigenvalues analysis for sensing deformation of wing frame using iFEM. *Sensors (Switzerland)* **2018**, *18*, doi:10.3390/s18082424.

49. Roy, R.; Tessler, A.; Surace, C.; Gherlone, M. Shape sensing of plate structures using the inverse finite element method: Investigation of efficient strain–sensor patterns. *Sensors (Switzerland)* **2020**, *20*, 1–24, doi:10.3390/s20247049.

50. Kefal, A.; Hizir, O.; Oterkus, E. A smart system to determine sensor locations for structural health monitoring of ship structures. *Int. Work. Sh. Mar. Hydrodyn.* **2015**, 26–28.

51. Tessler, A.; Riggs, H.R.; Macy, S.C. A variational method for finite element stress recovery and error estimation. *Comput. Methods Appl. Mech. Eng.* **1994**, *111*, 369–382, doi:10.1016/0045-7825(94)90140-6.

52. Riggs, H.R.; Tessler, A.; Chu, H. C1-continuous stress recovery in finite element analysis. *Comput. Methods Appl. Mech. Eng.* **1997**, *143*, 299–316, doi:10.1016/S0045-7825(96)01151-6.

53. Tessler, A.; Riggs, H.R.; Freese, C.E.; Cook, G.M. An improved variational method

for finite element stress recovery and a posteriori error estimation. *Comput. Methods Appl. Mech. Eng.* **1998**, *155*, 15–30.

54. Tessler, A.; Riggs, H.R.; Dambach, M. A novel four-node quadrilateral smoothing element for stress enhancement and error estimation. *Int. J. Numer. Methods Eng.* **1999**, *44*, 1527–1543.

55. Kefal, A.; Emami, I.; Yildiz, M.; Tessler, A. A smoothed iFEM approach for efficient shape-sensing applications : Numerical and experimental validation on composite structures. *Mech. Syst. Signal Process.* **2021**, *152*, 107486, doi:10.1016/j.ymssp.2020.107486.

56. Oboe, D.; Colombo, L.; Sbarufatti, C.; Giglio, M. Comparison of strain pre-extrapolation techniques for shape and strain sensing by iFEM of a composite plate subjected to compression buckling. *Compos. Struct.* **2021**, *262*, 113587, doi:10.1016/j.compstruct.2021.113587.

57. Mindlin, R.D. Influence of rotatory inertia and shear on flexural motions of isotropic, elastic plates. *J. Appl. Mech.* **1951**, *12*, 31–38.

58. Cook, R.D. Four-node 'flat' shell element: drilling degrees of freedom, membrane-bending coupling, warped geometry, and behaviour. *Comput. Struct.* **1994**, *50(4)*, 549–555.

59. Tessler, A.; Dong, S.B. On a hierarchy of conforming Timoshenko beam elements. *Comput. Struct.* **1981**, *14*, 335–344.

60. Tessler, A.; Hughes, T.J.R. An improved treatment of transverse shear in the mindlin-type four-node quadrilateral element. *Comput. Methods Appl. Mech. Eng.* **1983**, *39*, 311–335, doi:10.1016/0045-7825(83)90096-8.

61. Tessler, A. An efficient, conforming axisymmetric shell element including transverse shear and rotary inertia. *Comput. Struct.* **1982**, *15,* 567–574.